journal

J. Am. Ceram. Soc., 80 [1] 3–21 (1997)

# Three-Dimensional Computer Simulation of Portland Cement Hydration and Microstructure Development

Dale P. Bentz*

Building and Fire Research Laboratory, National Institute of Standards and Technology, Gaithersburg, Maryland 20899

**A three-dimensional computer model for the simulation of portland cement hydration and microstructure development has been developed. Starting with a measured particle-size distribution and a set of scanning electron microscopy images, a three-dimensional representation of a cement of interest is reconstructed, matching the phase volume fractions and surface-area fractions of the two-dimensional images. A set of cellular-automata rules is then applied to the starting microstructure to model the chemical reactions for all of the major phases during the evolving hydration process. The dissolution cycles used in the model have been calibrated to real time using a single set of parameters for two cements at three different water-to-cement ratios. Based on this calibration, there is excellent agreement between the model predictions and experimental measurements for degree of hydration, heat release, and chemical shrinkage. The degree-of-hydration predictions have been successfully applied to predicting the compressive strength development of mortar cubes for the two cements. The effects of temperature have been examined by performing hydration experiments at 15°, 25°, and 35°C and applying a maturity-type relationship to determine a single degree of hydration–equivalent time curve that can be compared to the model predictions. Finally, the computer model has been further extended to simulate hydration under sealed conditions, where self-desiccation limits the achievable hydration.**

## I. Introduction

As with any material, an understanding of the links between the microstructure of cement-based materials and their properties is needed to allow the design of systems with improved performance. Unfortunately, three-dimensional quantitative characterization of microstructure is extremely tedious and difficult. Although two-dimensional scanning electron microscopy (SEM) images of hydrated cement paste are straightforward to obtain, it is the three-dimensional microstructure that often has a critical influence on properties. Unlike phase volume fractions that are statistically the same in two and three dimensions for isotropic systems, the connectivity or percolation of phases is vastly different in two and three dimensions. Because percolation aspects are critical to the mechanical and transport properties of cementitious materials,[1,2] a three-dimensional representation of microstructure is required. Although difficult to obtain experimentally at the necessary resolution, such representations **can** be simulated using computer models.

Using computer models to represent the microstructure of cement-based materials has evolved significantly over the past 10 years or so, as reviewed in Panel A. In the present study, an experimental validation was conducted to determine the relationship between model cycles and real time for two cements at three different water-to-cement ($w/c$) ratios based on measurements of degree of hydration via nonevaporable water content, heat release, and chemical shrinkage. In addition, temperature effects and curing under sealed conditions were assessed experimentally for incorporation into the computer model. The overall model and experimental program are summarized in the flow diagram in Fig. 1.

## II. Experimental Procedures

### (1) Materials

The two cements selected for this study were issued as Cements 115 and 116 by the ASTM-sponsored Cement and Concrete Reference Laboratory (CCRL), located at the National Institute of Standards and Technology (NIST), as part of its proficiency sample program in January 1995. A sufficient supply of these cements stored in a double layer of plastic in

P. W. Brown—contributing editor

Manuscript No. 191768. Received June 3, 1996; approved September 9, 1996.
*Member, American Ceramic Society.

cardboard boxes was obtained for the present studies. The chemical compositions of the two cements, as determined in the proficiency sample program,[20] are given in Table I. Other results available in the CCRL summary report,[20] obtained using the indicated standard test methods,[21] include the initial and final times of set via the Vicat (ASTM C191[†]) and Gillmore (ASTM C266[†]) needle methods, measured finenesses (ASTM C204[†] and C115[†]), mortar cube compressive strengths (ASTM C109[†]), and heats of hydration at 7 and 28 d of age measured via the heat of solution method (ASTM C186[†]). The particle-size distributions for Cements 115 and 116 were measured at

[†]"Time of Setting of Hydraulic Cement by Vicat Needle," ASTM Designation C 191; "Calcium Sulfate in Hydrate Portland Cement Mortar," ASTM Designation C 266; "Fineness of Portland Cement by Air Permeability Apparatus," ASTM Designation C 204; "Fineness of Portland Cement by the Turbidimeter," ASTM Designation C 115; "Compressive Strength of Hydraulic Cement Mortars," ASTM Designation C 109; and "Heat of Hydration of Hydraulic Cement," ASTM Designation C 186. *1993 Book of ASTM Standards*, Vol. 04.01. American Society for Testing and Materials, Philadelphia, PA.

## Panel A: Computer-Based Microstructural Models of Cement and Concrete

Wittmann *et al.*[3,4] were perhaps the first to consider representing a cement or concrete microstructure numerically within a computer with the development of their "numerical concrete." A concrete microstructure consisting of aggregates in a cement paste matrix was generated and mapped onto a finite-element grid, allowing for the computation of thermal, hygral, and mechanical stress distributions. Each aggregate particle could be mapped onto one or more finite elements, so that this model represented the concrete at the subparticle level.

At the level of cement paste, pioneering work in directly representing the cement paste microstructure at the cement particle level was performed by Jennings and Johnson,[5] who developed a continuum representation based on spherical cement (tricalcium silicate, $C_3S$) particles enveloped by hydration shells of calcium silicate hydrate (C-S-H) gel, whose thickness increased over time. In addition, calcium hydroxide (CH) crystals were allowed to nucleate and grow in the continuum pore space. This model is classified as being of the continuum type, in that each particle can be described by its centroid location and a set of radii, corresponding to the unhydrated core and one or more shells of hydration products (representing inner and outer C-S-H product,[6] for example). A somewhat similar approach was formulated by van Breugel,[7,8] who, by accounting for the volumes of embedded cement particles and other morphological aspects of the hydrating cement paste system, was able to predict the hydration behavior, explicitly considering the cement particle-size distribution, its chemical composition, water-to-cement ($w/c$) ratio, and temperature. An example of the graphical output produced by this model, and quite similar to that first produced by the Jennings/Johnson model, can be found in Fig. A1. This approach is currently undergoing further development by other research groups.[9]

A second type of continuum model being used to generate cement microstructures is based on the mosaic method.[10] Here, a two-dimensional space is divided by a set of intersecting lines (planes would be used in three dimensions), and the resultant polygonal shapes taken to represent unhydrated cement particles and hydration products. Although multiple discrete phases can be modeled easily using this technique, simultaneously modeling multiple continuous or percolated phases, such as CH, capillary porosity, and C-S-H gel in cement paste, may present a computational challenge. In summary, continuum models can provide valuable quantitative information, such as the effects of particle size on hydration kinetics, but one finds it difficult to analyze such a microstructure to directly compute transport and elastic properties, such as can be easily computed for Wittmann's numerical concrete.

An alternate approach to continuum-based models has been the development of so called digital-image-based models.[2,11] These models operate at the subparticle level as each cement particle is represented as a collection of elements (pixels). Cement hydration can then be simulated by operating on the entire collection of pixels using a set of cellular-automata-like rules,[12] as illustrated in Fig. A2. This allows for the direct representation of multisize, multiphase, nonspherical cement particles. In two dimensions, a processed SEM image (as described in Panel B) can be used as direct input into the hydration model. The model has evolved from one based simply on the hydration of $C_3S$[13] to one that considers all of the major phases present in cement.[14] Recently, a similar two-dimensional model that emphasizes ion concentrations and diffusion processes has been developed.[15] Because of the underlying pixel representation of these microstructures, mapping the microstructure onto a finite-difference or finite-element grid becomes trivial, because there can be a simple one-to-one mapping between pixels and finite elements. Thus, properties such as percolation,[11] diffusivity,[16] complex impedance,[17] and setting behavior[2] are easily computable. The major limitation of digital-image-based models is perhaps one of resolution. Because each pixel is typically 1 $\mu m^3$ in volume, features smaller than this cannot be resolved. Fortunately, most cement particles are between 1 and 70 $\mu m$ in diameter, so that a given cement can be very accurately represented in a computational volume of 200 × 200 × 200 pixels. In addition, models at the micrometer level have been successfully integrated with others at the nanometer (C-S-H gel) and millimeter (mortar or concrete) level to provide a quantitative description of concrete microstructure that spans 7 orders of magnitude in scale.[18,19]

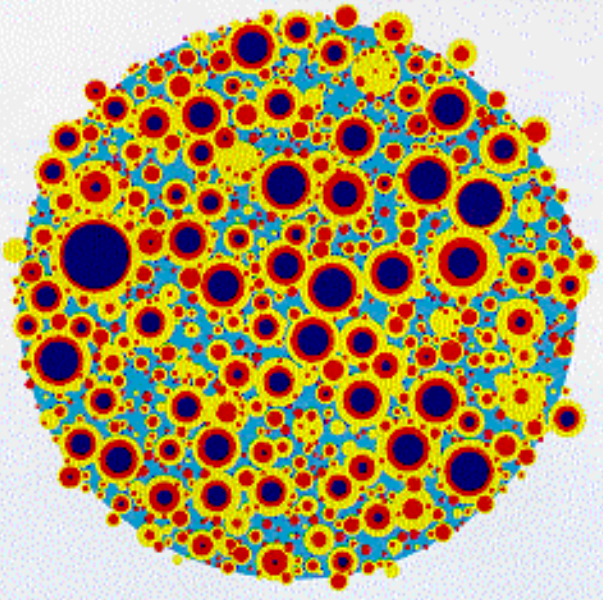

**Fig. A1.** Example of graphical output from the model of van Breugel. Image shown is a two-dimensional slice from a three-dimensional spherical computational volume (unhydrated cement cores are dark blue, inner C-S-H product is red, outer C-S-H product is yellow, and water-filled space is light blue). (Courtesy of K. van Breugel.)

**Panel A continued**

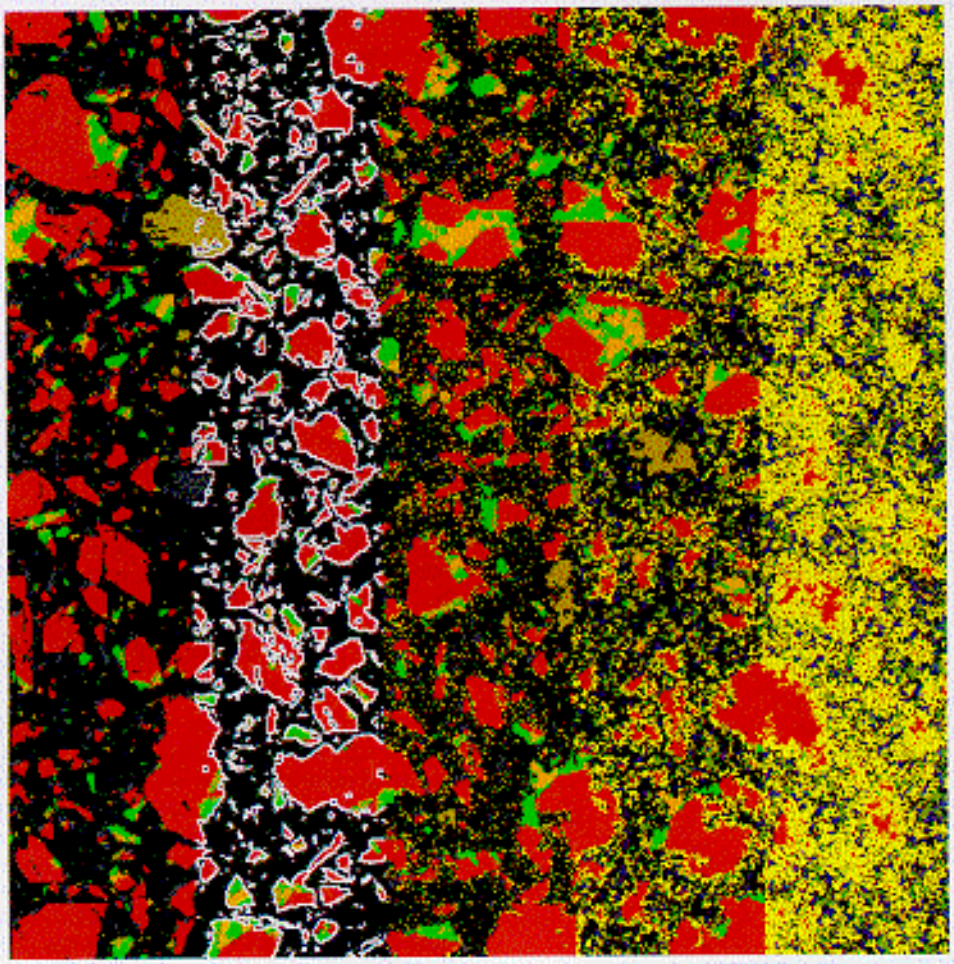

**Fig. A2.** Illustration of various steps in the digital-image-based cement hydration model showing, from left to right, initial cement particles in water (black), highlighting (white) of all cement particle surfaces in contact with water, generation of one-pixel diffusing species, and hydrated images at ~32% and 76% hydration, respectively ($C_3S$ is red, $C_2S$ is blue, $C_3A$ is bright green, $C_4AF$ is orange, gypsum is pale green, C-S-H is yellow, CH is dark blue, and aluminate hydration products (ettringite, monosulfoaluminate, and $C_3AH_6$) are green).

the University of Illinois using an X-ray sedigraph technique. The cumulative curves were discretized (binned) into 2 μm increments, resulting in the discrete distributions given in Table II, which were then used in the three-dimensional cement hydration model.

For the nonevaporable water content and chemical shrinkage determinations, cement pastes were prepared with *w/c* ratios of 0.30, 0.40, and 0.45. The cement powder and necessary mass of water were mixed together by kneading by hand in a sealed plastic bag for 2–3 min. For the studies at 15° and 35°C, a

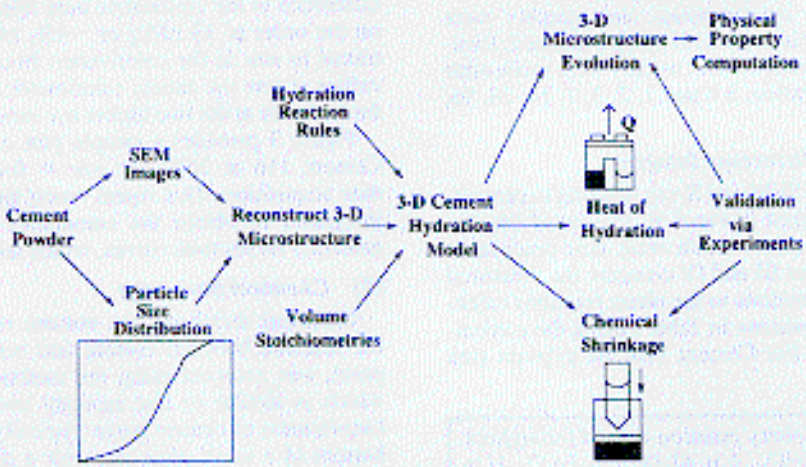


**Fig. 1.** Flow diagram summarizing experimental and modeling program for predicting cement performance.

**Table I. Oxide Compositions for CCRL Cements 115 and 116[20]**

| Oxide | Composition (mass%) Cement 115 | Cement 116 |
|---|---|---|
| CaO | 65.069 | 64.964 |
| $SiO_2$ | 21.479 | 20.572 |
| $Al_2O_3$ | 4.483 | 5.404 |
| $Fe_2O_3$ | 3.4686 | 1.9919 |
| $SO_3$ | 2.6733 | 2.9105 |
| MgO | 0.96 | 1.2781 |
| $K_2O$ | 0.16 | 0.656 |
| $Na_2O$ | 0.0741 | 0.1229 |
| Free lime | 0.497 | 0.987 |
| Loss on ignition | 1.0354 | 1.5252 |

**Table II. Discretized Particle-Size Distributions for CCRL Cements 115 and 116**

| Diameter (μm) | Mass fraction Cement 115 | Cement 116 |
|---|---|---|
| 3 | 0.162 | 0.245 |
| 5 | 0.136 | 0.153 |
| 7 | 0.125 | 0.122 |
| 9 | 0.075 | 0.087 |
| 11 | 0.095 | 0.107 |
| 13 | 0.064 | 0.077 |
| 15 | 0.056 | 0.038 |
| 17 | 0.053 | 0.036 |
| 19 | 0.044 | 0.039 |
| 21 | 0.041 | 0.046 |
| 23 | 0.036 | 0.005 |
| 25 | 0.036 | 0.023 |
| 27 | 0.021 | 0.000 |
| 29 | 0.015 | 0.004 |
| 31 | 0.015 | 0.013 |
| 33 | 0.012 | 0.005 |
| 35 | 0.003 | 0.000 |
| 37 | 0.01 | 0.000 |

walk-in environmental chamber was used so that the mixing could be performed at the desired temperature, after the starting materials had equilibrated in the chamber overnight. After they were mixed, the samples were removed and stored in capped plastic vials and small glass jars for the nonevaporable water content and chemical shrinkage measurements, respectively. For the chemical shrinkage studies and all saturated hydration experiments, after the cement paste sample (typically 10–15 g) was placed in its container, ~1 mL of water was added on top of the cement paste to maintain saturated conditions throughout the experiment. For the sealed hydration experiments, the plastic vials were capped with no addition of water. For the nonevaporable water content measurement, the samples were stored at the temperature of interest until being evaluated. Evaluations of nonevaporable water content usually were made after the following times of hydration: 8 h and 1, 2, 3, 7, 14, 28, 56, and 90 d.

### *(2) Scanning Electron Microscopy Imaging*

The recent application of SEM and X-ray imaging to cement-based materials is summarized in Panel B. Images of the two CCRL cements analyzed in this research using these procedures are provided in Fig. 2. Tables III and IV compare the measured area and perimeter phase fractions to the phase fractions calculated from the oxide compositions in Table I using the conventional Bogue calculation.[26] For Cement 116, the gypsum area fraction is somewhat high because of the presence of a large gypsum particle in the field of view selected for analysis, as shown in Fig. 2.

Conventional cement chemistry notation is used throughout this paper: C is CaO, S is $SiO_2$, A is $Al_2O_3$, F is $Fe_2O_3$, H is $H_2O$, and $\bar{S}$ is $SO_3$.

### *(3) Degree of Hydration—Nonevaporable Water Content*

After achieving the required age, samples for the nonevaporable water content ($W_N$) determination were ground to a powder using a mortar and pestle and washed with methanol, using a porous ceramic filter and a vacuum, to stop the hydration. The resultant powder was divided approximately in half and placed in two crucibles of known mass and left overnight (on the order of 20 h) in an oven at 105°C. When they were removed from the oven, the masses of the crucibles and samples were redetermined before placing them in a furnace at 950°C for a minimum of 4 h, after which their masses once again were determined. The nonevaporable water content was calculated as the difference between the 950° and 105°C mass measurements divided by the mass of cement remaining at 950°C, corrected for the loss on ignition of the cement powder itself, which was assessed in a separate crucible experiment. Based on the expected uncertainty of the mass measurements (0.001 g), a typical expanded uncertainty[27] in the calculated $W_N$ is estimated to be 0.001 g of $H_2O$/(g of cement), assuming a coverage factor[27] of 2. The nonevaporable water contents were converted to degrees of hydration by normalizing by the values measured for fully hydrated samples of the two cements,[14] 0.226 and 0.235 g of $H_2O$/(g of cement) for Cements 115 and 116, respectively.

### *(4) Heat of Hydration*

The heats of hydration of the two cements were assessed using a multichambered microcalorimeter constructed at NIST.[28] A known mass of cement and several small stainless-steel balls to facilitate mixing were placed in a sealed calorimeter cell that was then equilibrated in the main calorimeter chamber. After a steady heat flux signal was obtained, the cell was removed, the appropriate mass of water (also thermally equilibrated to the calorimeter temperature) quickly added using a syringe, and hand mixing performed (by shaking the cell) before restoring the cell to the calorimeter chamber. The voltage signals produced (proportional to heat flux) by the calorimeter cells were digitized using a PC-based high-resolution analog-to-digital (A/D) data acquisition system. Thus, during the initial hydration, data could be taken at 30 s intervals. Once the reactions slowed, data were typically acquired every 5 or 10 min over a period of at least 7 d. At longer times, the signal of the calorimeter was very close to its background level, so that detection of the slow but ongoing hydration became unreliable. In analyzing the heat release data, the initial exothermic "mixing" peak was ignored because of the necessity of removing the sample cell from the calorimeter chamber to assure adequate mixing. This was considered to be the major contribution to the uncertainty in the heat of hydration measurements and could result in a difference in the cumulative heat released over a period of 7 d on the order of 10 kJ/kg or ~4%, as estimated from samples mixed *in situ* in the calorimeter. Because of the mixing difficulties at low *w/c* ratios, calorimetric measurements were performed only at the two higher *w/c* ratios of 0.40 and 0.45.

Figure 3 provides a sample plot of the obtained signal for Cement 116 at 25°C for $w/c = 0.40$ for the first 24 h of data acquisition. This signal versus time was then numerically integrated to obtain the cumulative heat release (kJ/(kg of cement)) versus time curves, which are presented in the results.

### *(5) Chemical Shrinkage*

Chemical shrinkage, the volume reduction associated with the reaction between cement and water in hydrating cement paste, was assessed using the method described by Geiker,[29] which is similar to that recently used by Tazawa *et al.*[30] A known mass of cement paste (typically 10 g) was placed in the bottom of a small glass jar, with a diameter of 2.5 cm and a height of ~6 cm. After the cement paste was covered with ~1 mL of water, the remainder of the jar was filled with a

## Panel B: SEM and X-ray Imaging of Cement

There have been significant developments in recent years in the application of SEM and X-ray imaging to the characterization of cement-based materials. Because the flux of backscattered electrons (BSE) produced by the incident electron beam in the SEM is proportional to the average atomic number of a phase, in a BSE image of unhydrated cement particles, the $C_4AF$ phase, having the highest average atomic number, shows up as the brightest phase and is easily distinguishable from the other phases. Unfortunately, the other major phases, although exhibiting some contrast differences (i.e., the $C_3S$ being brighter than the others), cannot be reliably distinguished based solely on a BSE image. However, the X-rays emitted when the incoming electron beam interacts with the specimen surface provide valuable chemical information on the underlying phases, to supplement the BSE image. Typically, X-ray images are collected either as a binary dot map image (where all pixels exhibiting an X-ray intensity in a specific energy window that is greater than a preset threshold are set to a value of 255, for example) or as a continuous-valued X-ray image in which each pixel is assigned a 0–255 value based on the X-rays counts within some preset energy window. Using the X-ray techniques, resolution is typically limited to ~1 μm, which is smaller than the size of nearly all cement particles and fortuitously provides a scale identical to that commonly used in the NIST cement hydration model.

Several examples of applying these combined SEM techniques to cement-based materials can be found in recent literature. Scrivener[22] has collected X-ray dot map images for silicon and aluminum for several cements and processed them to determine the proportions of silicates and interstitial (aluminate) phases present overall and present on the surfaces of the cement particles. These results have been applied to interpreting the hydration characteristics of these cements as quantified by calorimetric heat-release measurements. Stutzman[23] has collected X-ray map images for calcium, silicon, aluminum, and iron for cement clinkers (prior to grinding) and computed the area fractions of each of the four major clinker phases. For example, image areas containing calcium and aluminum, but no iron, were assigned to be the $C_3A$ phase. Bonen and Diamond[24] have quantified the effects of grinding techniques on cement particle size, shape, and phase distribution, using SEM and X-ray analysis to classify the predominant phase found in each cement particle.

By applying these techniques to each pixel in an image, as opposed to each particle, Bentz and Stutzman[25] have been able to map each pixel to its component phase. To perform this analysis, the cement of interest is first dispersed in a low-viscosity epoxy, which is subsequently cured. A polished surface is then prepared and viewed by SEM. For this application, in addition to the BSE image, X-ray images are collected for calcium, silicon, aluminum, iron, and sulfur. The uniqueness of this mapping is shown in a false-color image in which the calcium, silicon, and aluminum X-ray signals are assigned to the red, green, and blue color channels, respectively, as shown in Fig. B1 for Cement 115. The figure clearly shows the presence of two levels of yellow/orange, distinguishing the $C_3S$ phase from the $C_2S$ phase, due to a different calcium/silicon (red/green) ratio. Red areas indicate the presence of either gypsum or free lime (CaO), with the sulfur X-ray image being used to distinguish between the two. Magenta areas indicate the presence of both calcium and aluminum, with the BSE or iron X-ray images then being used to distinguish $C_4AF$ from $C_3A$. Although, in the current study, no attempt is made to distinguish the alkali sulfates from the gypsum, X-ray images of potassium and sodium could be collected easily and used for this purpose.

Because of the inherent noise in the X-ray images, after an initial segmentation is performed, a type of median filtering is applied to smooth the image. Here, each nonporosity pixel is replaced by the majority solid phase present in a limited neighborhood (e.g., 3 × 3) centered at the pixel. The image produced by this median filtering process can then be analyzed to determine phase area fractions, the perimeter fraction of each phase in contact with porosity, and the two-dimensional correlation function for any individual or combination of phases. This quantitative spatial information then can be utilized in reconstructing a three-dimensional representation of the cement of interest.

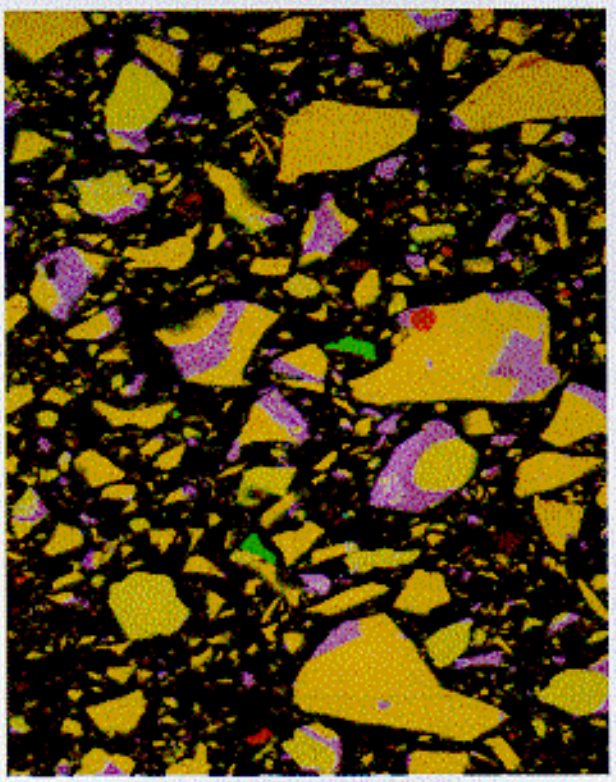

**Fig. B1.** False-color two-dimensional image of cement particles for Cement 115 with X-ray signal to color mappings of calcium to red, silicon to green, and aluminum to blue.

hydraulic oil. The jar was then sealed with a rubber stopper encasing a pipette graduated in 0.01 mL increments. The jar was then placed in a constant-temperature water bath ($T$ = 25°C), and the oil level within the pipette was measured to the nearest 0.0025 mL over time, typically for a period of 28 d. A control sample using only cement powder and oil (no water) was used to correct for minor room-temperature fluctuations. By normalizing the change in volume by the mass of cement in the sample, the chemical shrinkage per gram of initial cement (mL/(g of cement)) could be determined. Based on the estimated uncertainty of the mass (0.02 g) and volume (0.000 72 mL) measurements, the maximum expanded uncertainty[27] in the calculated chemical shrinkage was estimated to be 0.001 mL/(g of cement), assuming a coverage factor[27] of 2. In all cases, two specimens were run for each *w/c* ratio and cement, with the average result being reported.

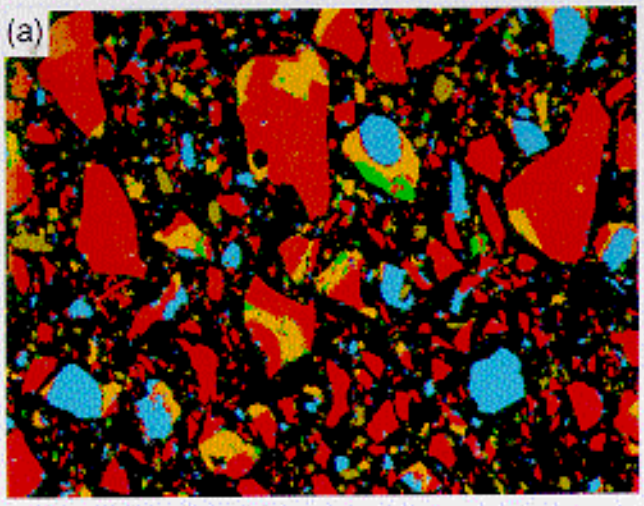


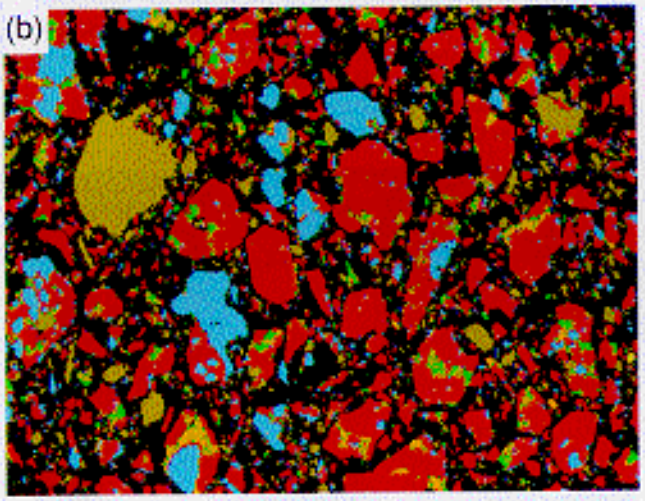


Fig. 2. Two-dimensional segmented images of (a) Cement 115 and (b) Cement 116 ($C_3S$ is red, $C_2S$ is aqua, $C_3A$ is green, $C_4AF$ is orange, and gypsum is pale green).

Table III. Phase Fractions for CCRL Cement 115

| Phase | Perimeter fraction | Area fraction | Bogue volume fraction |
|---|---|---|---|
| $C_3S$ | 0.504 | 0.605 | 0.547 |
| $C_2S$ | 0.239 | 0.221 | 0.214 |
| $C_3A$ | 0.045 | 0.032 | 0.081 |
| $C_4AF$ | 0.076 | 0.097 | 0.093 |
| Gypsum | 0.136 | 0.046 | 0.065 |

Table IV. Phase Fractions for CCRL Cement 116

| Phase | Perimeter fraction | Area fraction | Bogue volume fraction |
|---|---|---|---|
| $C_3S$ | 0.399 | 0.575 | 0.544 |
| $C_2S$ | 0.242 | 0.190 | 0.195 |
| $C_3A$ | 0.084 | 0.061 | 0.137 |
| $C_4AF$ | 0.020 | 0.031 | 0.054 |
| Gypsum | 0.255 | 0.142 | 0.071 |

## III. Computational Techniques

### (1) Three-Dimensional Reconstruction

Although two-dimensional images of cement particles are useful for characterizing cements, three-dimensional representations are necessary to obtain hydrated microstructures for the computation of percolation, mechanical, and transport properties. Recently, computational techniques have been developed for creating three-dimensional cement particle images that match the following characteristics of the cement of interest: particle-size distribution, phase volume fractions, and phase surface-area fractions.[14] The latter two of these characteristics are determined based on analysis of a two-dimensional cement particle image. In addition, the autocorrelation functions[31] for each phase and different groupings of phases are used during the three-dimensional reconstruction process to match the correlation structure of the phases within the three-dimensional cement particles to their two-dimensional counterpart.

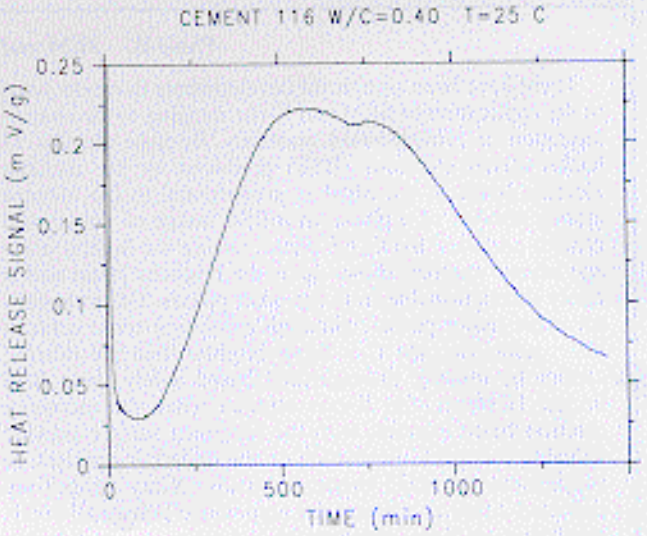


Fig. 3. Experimental heat release signal versus time.

Initially, digitized spherical particles matching the particle-size distributions given in Table II, at a resolution of 1 μm/pixel, are placed from largest to smallest at random locations into a three-dimensional computational volume 100 pixels on a side, using periodic boundary conditions. A fraction of the particles are assigned to be gypsum (to match the gypsum volume fraction of the cement), with the remainder being designated as cement and later separated into distinct phase regions using the algorithm described below. Thus, we are explicitly assuming that the gypsum and the cement particles follow the same particle-size distribution. Because no superplasticizer or water-reducing agent has been used in the experimental studies, after random placement, the particles are flocculated into a single floc structure by randomly displacing their centroids by a distance of one pixel in one of six random directions ($\pm x$, $\pm y$, $\pm z$) and moving all contacting particles as a single unit in subsequent iterations of the algorithm.[2,14]

To begin the phase segmentation of the three-dimensional particle image, the two-point correlation function is determined for three different phase combinations[14] in the final two-dimensional segmented SEM image: the combined silicates, the $C_3S$, and either the $C_3A$ or the $C_4AF$ (whichever is the more abundant of the two). This function is evaluated for an $M \cdot N$ image using the following equation:

$$S(x,y) = \sum_{i=1}^{M-x} \sum_{j=1}^{N-y} \frac{I(i,j)\, I(i+x, j+y)}{(M-x)(N-y)} \tag{1}$$

where $I(x,y) = 1$ if the pixel at location $(x,y)$ contains the phase(s) of interest and $I(x,y) = 0$ otherwise. These values are then converted to $S(r)$ for distances $r$ in pixels by[31]

$$S(r) = \frac{1}{2r+1} \sum_{t=0}^{2r} S\left(r, \frac{\pi t}{4r}\right) \tag{2}$$

where, for angles $t$, $S(r,t) = S(r \cos t, r \sin t)$ is obtained by bilinear interpolation from the values of $S(x,y)$.

The two-point correlation function for the silicates is used to separate the cement particles into silicates and aluminates. To do this, each pixel in the three-dimensional cement particle image is assigned a random number following a normal distribution ($N(x,y,z)$) generated using the Box–Muller method.[32] This random number image is then filtered using the autocorrelation function ($F(x,y,z)$):

$$F(r) = F(x,y,z) = \frac{S(r = (x^2+y^2+z^2)^{1/2}) - S(0)\,S(0)}{S(0) - S(0)\,S(0)} \tag{3}$$

The resultant image ($R(x,y,z)$) is calculated as

$$R(x,y,z) = \sum_{i=0}^{30}\sum_{j=0}^{30}\sum_{k=0}^{30} N(x+i,y+j,z+k)\,F(i,j,k) \tag{4}$$

Finally, for those pixels in the resultant image originally assigned to be the phase(s) of interest (cement in this first case), a threshold operation is performed to create the appropriate volume fractions of the two phases. For example, if a cement pixel of interest has an $R$-value above a critical threshold, it is reassigned to be the aluminate phase. If not, it is assigned to be the silicate phase. The critical threshold value is determined such that, after the threshold operation, the fraction of pixels that has been reassigned corresponds to the desired volume fraction for the reassigned phase (based on analysis of the two-dimensional SEM images).

After this algorithm is executed to separate the cement (non-gypsum) particles into silicates and aluminates, the appropriate volume fractions of these two "phases" exist in the generated three-dimensional image. However, it remains to match the surface-area fractions as well. To do this, a pixel rearrangement algorithm, based on analysis of local three-dimensional curvature,[33,34] is used. The local curvature is defined simply to be proportional to the fraction of pixels in some local neighborhood (e.g., a 3 × 3 × 3 box or sphere) that is assigned to be porosity. Here, pixels of one solid phase located at high-curvature sites are exchanged with pixels of the other solid phase located at low-curvature sites. This changes the fraction of each phase in contact with the pore space so that the surface-area fractions of each phase can be made to match the perimeter fractions present in the original two-dimensional SEM image.

Once this phase separation is accomplished for converting the "cement" into the silicates and aluminates, the algorithms are executed on the developing three-dimensional image two more times. The silicates are further segmented into $C_3S$ and $C_2S$, whereas the aluminates are further divided into $C_3A$ and $C_4AF$. Figure 4 shows a portion of an initial generated three-dimensional microstructure for Cement 115 at a $w/c$ ratio of 0.40.

### (2) *Three-Dimensional Cement Hydration Model*

The cement hydration model was originally developed in two dimensions[12] to operate directly on SEM images such as those in Fig. 2. Recently, the model was extended to three dimensions; additions were made to determine model heat of hydration and chemical shrinkage; and the densities/molar volumes of C-S-H, ettringite, and iron hydroxide were adjusted to better model the experimental data generated for actual cements.[14] To begin, one must decide the phases and reactions to consider in the cement hydration model. Table V provides a list of the phases included in the present version of the three-dimensional cement hydration model, with their densities, molar volumes,[35,36] and heats of formation.[37,38] Figure 5 summarizes the reactions included in the current version of the model, as modified from those provided previously.[12] The volume stoichiometries indicated below each reaction have been calculated based on the molar stoichiometries of the reactions and the compound molar volumes tabulated in Table V. For C-S-H, the density and molar volume given in Table V were obtained by calibrating measured chemical shrinkage to that predicted by the model,[14] because the values given in the literature[36] for these properties predict

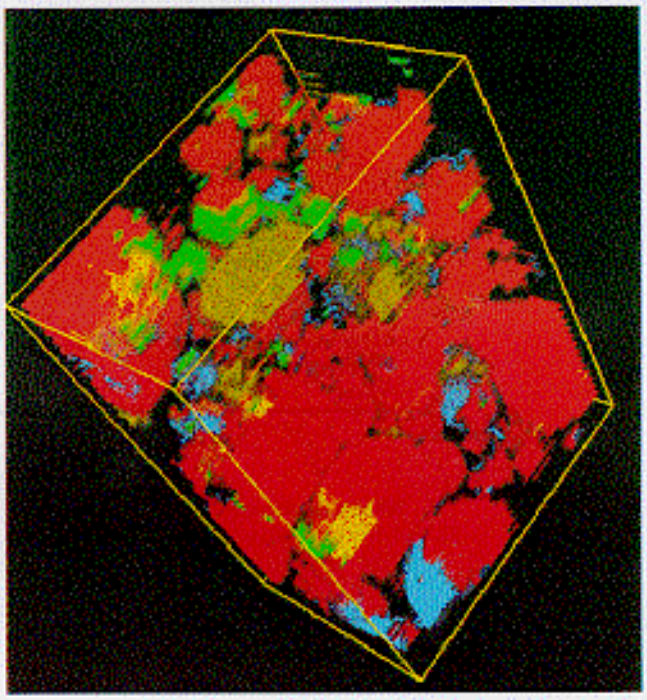

**Fig. 4.** Portion of a reconstructed three-dimensional starting image for Cement 115 with $w/c = 0.40$ ($C_3S$ is red, $C_2S$ is aqua, $C_3A$ is green, $C_4AF$ is orange, and gypsum is pale green).

no chemical shrinkage for the hydration of $C_3S$ and $C_2S$, in contrast to the experimentally observed behavior.[39] For both $C_3S$ and $C_2S$ hydration, the values given in Table V result in chemical shrinkages of −6.7 g of $H_2O$/(g of cement) at complete hydration, in reasonable agreement with the value of 5.3 g of $H_2O$/(g of cement) measured by Powers[39] for $C_3S$ after 28 d hydration.

The reactions provided in Fig. 5 are implemented as a series of cellular automata-like rules (see Panel C for a brief introduction to cellular-automata) that operate on the original three-dimensional representation of cement particles in water. Rules are provided for the dissolution of solid material, diffusion of the generated diffusing species, and reactions of diffusing species with each other and with solid phases. These rules are summarized in the state transition diagram provided in Fig. 6. Their implementation is as follows.

For dissolution, first, an initial scan is made through all pixels (elements) present in the three-dimensional microstructure, to identify all pixels that are in contact with pore space. Thus, any solid pixels that have one or more immediate (±1 in the $x$, $y$, or $z$ directions) neighbors that are classified as porosity are eligible for dissolution. In addition, each solid phase is characterized by two dissolution parameters, a solubility flag and a dissolution probability. The solubility flag indicates if a given phase is currently soluble during the hydration process, with a value of 1 indicating that the phase is soluble. The initial cement phases always are soluble during the hydration process. Conversely, some phases, such as ettringite, are initially insoluble but become soluble during the hydration (e.g., when the gypsum is nearly consumed). The calcium hydroxide also is soluble to allow Ostwald ripening of the smaller calcium hydroxide crystals into larger ones. The second parameter indicates the relative probability of a phase dissolving when a pixel containing that phase "steps" into pore space. This is included in the model to allow the cement minerals to react at different rates, as has been observed experimentally.[35] In the current model configuration, $C_3A$ and $C_3S$ are assigned dissolution probabilities 5–8 times greater than those given $C_4AF$ and $C_2S$. Because the latter two phases generally account for <30% of the cement, variations in their dissolution probabilities do not have a major effect on the

**Table V. Physical Properties of Cementitious Materials**

| Compound name | Compound formula | Density ($Mg/m^3$) | Molar volume ($cm^3/mol$) | Heat of formation (kJ/mol) |
|---|---|---|---|---|
| Tricalcium silicate | $C_3S$ | 3.21 | 71. | −2927.82 |
| Dicalcium silicate | $C_2S$ | 3.28 | 52. | −2311.6 |
| Tricalcium aluminate | $C_3A$ | 3.03 | 89.1 | −3587.8 |
| Tetracalcium aluminoferrite | $C_4AF$ | 3.73 | 128 | −5090.3 |
| Gypsum | $C\bar{S}H_2$ | 2.32 | 74.2 | −2022.6 |
| Calcium silicate hydrate | $C_{1.7}SH_4$ | 2.12 | 108 | −3283. |
| Calcium hydroxide | CH | 2.24 | 33.1 | −986.1 |
| Ettringite | $C_6A\bar{S}_3H_{32}$ | 1.7 | 735. | −17539. |
| Monosulfate | $C_4A\bar{S}H_{12}$ | 1.99 | 313. | −8778. |
| Hydrogarnet | $C_3AH_6$ | 2.52 | 150. | −5548. |
| Iron hydroxide | $FH_3$ | 3.0 | 69.8 | −823.9 |
| Water | H | 1.0 | 18.0 | −285.83 |

**Silicate Reactions**

$$C_3S + 5.3H \rightarrow C_{1.7}SH_4 + 1.3CH$$
1 1.34 1.521 0.61

$$C_2S + 4.3H \rightarrow C_{1.7}SH_4 + 0.3CH$$
1 1.49 2.077 0.191

**Aluminate and Ferrite Reactions**

$$C_3A + 6H \rightarrow C_3AH_6$$
1 1.21 1.69

$$C_3A + 3C\bar{S}H_2 + 26H \rightarrow C_6A\bar{S}_3H_{32}$$
0.4 1 2.1 3.3

$$2C_3A + C_6A\bar{S}_3H_{32} + 4H \rightarrow 3C_4A\bar{S}H_{12}$$
0.2424 1 0.098 1.278

$$C_4AF + 3C\bar{S}H_2 + 30H \rightarrow C_6A\bar{S}_3H_{32} + CH + FH_3$$
0.575 1 2.426 3.3 0.15 0.31

$$2C_4AF + C_6A\bar{S}_3H_{12} + 12H \rightarrow 3C_4A\bar{S}H_{12} + 2CH + 2FH_3$$
0.348 1 0.294 1.278 0.09 0.19

$$C_4AF + 10H \rightarrow C_3AH_6 + CH + FH_3$$
1 1.41 1.17 0.26 0.545

**Fig. 5.** Cement model reactions (numbers below reactions indicate volume stoichiometry).

results of the hydration model, although recent research has shown that enhancing the dissolution of $C_4AF$ can significantly influence the properties of cements with substantial $C_4AF$ fractions.[46]

In a second pass through the microstructure, all identified surface pixels are allowed to take a one-step random walk. If the step lands the pixel in porosity, the phase comprising the pixel is currently soluble, and dissolution is determined to be probable (by comparing a uniform random number between 0 and 1 to the dissolution probability), the dissolution is allowed, and one or more diffusing species are generated, as indicated in Fig. 6. These diffusing species are **not** individual ions but, rather, represent a collection of ions that occupy one pixel ($\sim 1\ \mu m^3$) unit of volume, consistent with a cellular-automata approach to modeling microstructure development.[12] If the dissolution is not allowed, the surface pixel simply remains as its current solid phase, but it may dissolve later in the hydration. The locations of all diffusing species are stored in a linked list data structure that can expand and contract dynamically during execution to optimize memory usage.[47] In this way, unlike in previous versions of the NIST hydration model,[12,13] diffusing species may remain in solution from one dissolution step to the next. Previously, all diffusing species were reacted before a new dissolution step was performed.

The generated diffusing species execute random walks in the available pore space, until they react according to the rules provided in Fig. 6. For each diffusing species, the reaction rules included in the present version of the three-dimensional cement hydration model are as follows.

(1) Diffusing C-S-H: When a diffusing C-S-H species collides with either solid $C_3S$ or $C_2S$ or previously deposited C-S-H, it is converted into solid C-S-H with a probability of 1.

(2) Diffusing CH: For each diffusion step, a random number is generated to determine if nucleation of a new CH crystal is probable; if so, the diffusing CH is converted into solid CH at its present location. In addition, if a diffusing CH collides with solid CH, it is converted into solid CH with a probability of 1.

(3) Diffusing $FH_3$: For each diffusion step, a random number is generated to determine if nucleation of a new $FH_3$ crystal is probable; if so, the diffusing $FH_3$ is converted into solid $FH_3$ at its present location. In addition, if a diffusing $FH_3$ collides with solid $FH_3$, it is converted into solid $FH_3$ with a probability of 1.

(4) Diffusing gypsum: The diffusing gypsum can react only by collision with some other species in the microstructure. If it collides with solid C-S-H, it can be absorbed if the previously absorbed gypsum is less than some constant (e.g., 0.01) multiplied by the number of solid C-S-H pixels currently present in the system. If it collides with either solid or diffusing $C_3A$, ettringite is formed. If it collides with solid $C_4AF$, ettringite, CH, and $FH_3$ are formed to maintain the appropriate volume stoichiometry, as shown in Fig. 5.

(5) Diffusing ettringite: When diffusing ettringite is created, it also reacts only by collision with other species. If it collides with solid or diffusing $C_3A$, monosulfoaluminate is formed. If it collides with solid $C_4AF$, monosulfoaluminate, CH, and $FH_3$ are formed. Finally, if it collides with solid ettringite, there is a small probability that it is converted back into solid ettringite. This latter rule is provided to avoid the possibility of a large buildup of diffusing ettringite in the microstructure.

(6) Diffusing $C_3A$: If nucleation is probable or the diffusing $C_3A$ collides with solid $C_3AH_6$ and precipitation is probable, solid $C_3AH_6$ is formed. If it collides with diffusing gypsum, ettringite is formed. If it collides with diffusing or solid ettringite and ettringite is currently soluble, monosulfoaluminate is formed.

For $C_3AH_6$, CH, and $FH_3$, the probability of nucleation ($P_{nuc}$) of diffusing species is governed by an equation of the form

$$P_{nuc}(C_i) = A_i[1 - \exp(-[C_i]/[B_i])] \quad (5)$$

where $C_i$ is the current number of diffusing species $i$, and $A_i$ and $B_i$ constants that control the number and formation rate of crystals. This results in the effect that few new crystals are formed late in the hydration when the "concentrations" of diffusing species are reduced relative to their initial values, in agreement with experimental observations.[48]

In general, the hydration reaction products are allowed to grow with a completely random morphology. An exception to this is ettringite, where an attempt is made to grow the solid

### Panel C: Cellular-Automata

A cellular-automata (*CA*) is basically a computer algorithm that is discrete in space and time and operates on a lattice of sites[40,41] (i.e., a two-dimensional or three-dimensional array of pixels). Starting from some initial configuration, at each iteration of the algorithm, the state (value) of each site is updated based on its current value and the current value(s) of one or more neighboring sites. The evolution of the system structure (microstructure in our case) over a series of iterations (time) then is monitored in terms of both the visual appearance of the system and any number of global or local properties, such as phase volume fractions or percolation characteristics. The state space of each lattice site is usually limited to a few values; for the cement hydration model, this state space is comprised of individual values (integers) corresponding to each solid phase (including water) and each possible diffusing species. Update rules for dissolution and diffusion/reaction are then implemented as part of the computer algorithm, as illustrated in Fig. C1. Here, for the center pixel in the 3 × 3 grid, a random direction is chosen ($\pm x$, $\pm y$), with the *CA* outcomes shown for each of the four possible choices.

The cement hydration model is not a pure *CA* because nonlocal information is often used in determining the state space evolution (e.g., using a global concentration of a diffusing species to determine the likelihood of the nucleation of a new crystal), but is largely based on principles utilized in *CA*. Using a graphics workstation to implement the *CA* for cement hydration in real time provides the added advantage of visualization of the ongoing hydration process, extremely useful for debugging purposes and for gaining new insights into the effects of the selected rules on the evolving microstructure.

Although often relatively simple in structure, the behavior produced by *CA* can be quite complex. The field of *CA* has been developing over the past 10 years[40,41] or so, with recent applications in materials science (sintering[33,42] and dendritic growth[43,44]) and biological systems.[45]


Fig. C1. Illustration of the simple *CA* algorithms used for dissolution and diffusion/reaction in the cement hydration model. In far left images, central pixel being considered is marked with an X. Images to the right then show the resultant systems for each of the four possible chosen directions for dissolution/diffusion (red is solid material, green is water-filled porosity, and blue is diffusing species).

ettringite as needlelike structures by evaluating the surface curvature using a pixel-counting algorithm.[33,34] When new ettringite is forming, an attempt is made to maximize the number of non-ettringite pixels in contact with the new ettringite pixel. This naturally results in the formation of needlelike ettringite structures.

Prior to each dissolution, the three-dimensional microstructure is scanned to determine the number of pixels of each phase currently present in the system. From these volumes, chemical shrinkage and heat of hydration can be calculated. The chemical shrinkage is calculated by determining the amount of water consumed by reaction (based on the values in Table V and the reactions in Fig. 5) in comparison to the volume of capillary porosity remaining in the microstructure. For low *w/c* ratio systems, all of the water may be consumed while some capillary porosity remains. For those experiments conducted in this study for which hydration was executed under saturated conditions, simulations were performed assuming that external water always was available to fill the pores emptied by the chemical shrinkage. Thus, all porosity remained water filled during the complete execution of the hydration model. However, the model has been further extended to consider hydration under sealed conditions. To do this, prior to each new dissolution cycle, the volume of remaining porosity is compared to the volume of remaining water. The difference in these two values is converted into a number of porosity pixels to be converted

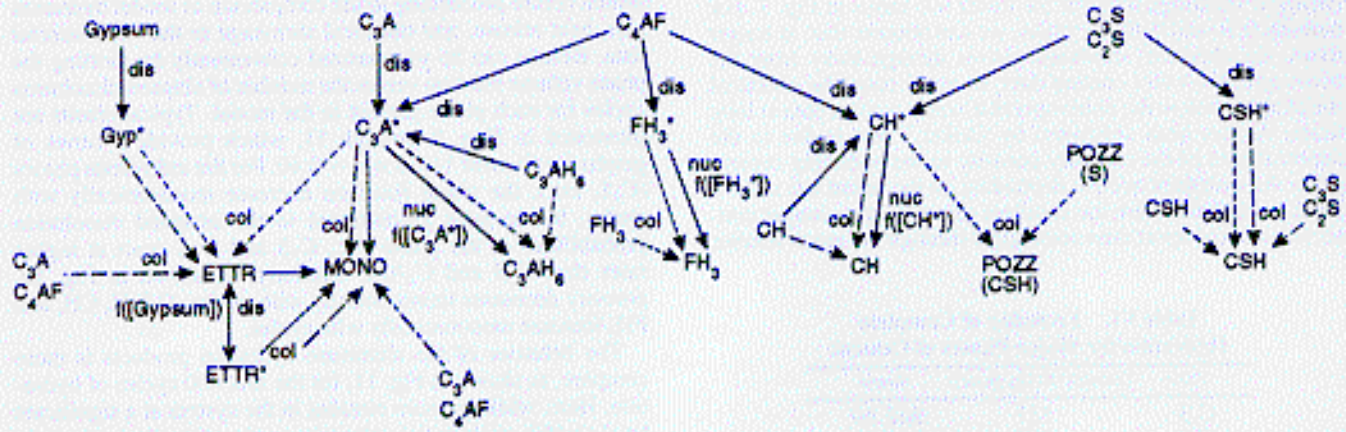


Fig. 6. State transition diagram for three-dimensional cement hydration model. Arrow patterns denote the collision of two species to form a hydration product. $f([X])$ denotes that nucleation or dissolution probability is a function of concentration or volume fraction of phase $X$. Asterisk (*) indicates diffusing species. ETTR is ettringite, MONO is monosulfate, pozz is pozzolanic material (silica fume, etc.). Gyp is gypsum, col is collision, nuc is nucleation, and dis is dissolution.

into empty porosity. In an attempt to simulate the actual physical process of pore emptying, the three-dimensional microstructure is then scanned to identify the largest water-filled pore regions (using different-sized spherical templates), which then are emptied sequentially from largest to smallest until the correct number of empty pore pixels has been created. In this way, the effects of self-dessication on the evolving hydration process can be simulated to compare to the experimental measurements of degree of hydration versus time.

The heat of hydration can be computed based on the heats of formation given in Table V or the tabulated enthalpy values for each of the four major phases as listed in Table VI. For the model, degree of hydration is calculated as the mass of cementitious material that has reacted divided by the starting mass of cement, with the conversion from a volume basis being performed using the densities of the starting materials given in Table V.

## IV. Results

### (1) Comparison of Experimental Measurements

Figure 7 provides a plot of the normalized experimental results for Cements 115 and 116 for *w/c* ratios of 0.30, 0.40, and 0.45 at $T = 25°C$. In this figure, the heat of hydration values have been normalized by the values calculated based on the Bogue potential phase compositions of the cements and the tabulated heats of hydration of the major phases provided in Table VI. The nonevaporable water contents have been normalized by the values measured experimentally on high *w/c* mixes.[14] Finally, the chemical shrinkage values have been normalized by the value (within ±0.01 mL/(g of cement)) that gives the best fit to the nonevaporable water content data for the *w/c* = 0.45 systems. The *w/c* = 0.45 data have been chosen because these results should not be affected by the depercolation of the capillary porosity, as discussed below. This value then is held constant at the lower *w/c* ratios. As shown in Fig. 7, excellent agreement is observed between the three measured properties, except for the lower *w/c* ratios at longer times, as explained below. A previous study by Parrott *et al.*[49] has produced similar agreement, finding "a directly proportional relationship between the heat of hydration and chemical shrinkage." Geiker[29] has noted a linear relationship between chemical shrinkage and nonevaporable water content for an ordinary portland cement with *w/c* = 0.5, cured at 20°C. In addition, in 1935, Powers[39] reported a linear relationship between heat of hydration and water absorbed during hydration for four different cements, with a constant of proportionality of 19.3 (cal/g)/(g of water/(100 g of cement)). For the results in Fig. 7, we find values of 16.9 ± 0.9 and 20.6 ± 0.9 for Cements 115 and 116, respectively, in good agreement with Powers' results.

One interesting observation can be made concerning the chemical shrinkage data for the lower *w/c* ratios in Fig. 7. For both the 0.30 and 0.40 *w/c* ratios, we can observe that, at longer times, the chemical shrinkage curves diverge away from the nonevaporable water content data. In every case, the chemical shrinkage is below the nonevaporable water content data at long times. As has been suggested by Geiker,[29] this is due to the depercolation of the capillary porosity in the hydrating cement paste. As hydration occurs, depending on the initial *w/c* ratio, a point is reached where the capillary porosity is no longer connected, and transport then must occur through the much smaller gel pores in the C-S-H gel.[11] Because this transport occurs at a much slower rate, the rate at which water is absorbed into the specimen falls below the rate at which empty voids are being generated, leading to the observed divergence in the experimental curves. The horizontal lines provided in Fig. 7 indicate the degree of hydration needed to achieve this capillary pore discontinuity, based on results from the original $C_3S$ hydration model.[11,13] The agreement between the experimental observations and the predicted point of discontinuity is quite good, particularly for the *w/c* = 0.30 data sets. This pore discontinuity also has been observed recently using impedance spectroscopy measurements on partially frozen cement paste specimens.[50]

**Table VI. Enthalpy of Complete Hydration for Major Phases of Cement**

| Phase | Enthalpy (kJ/(kg phase)) | Source |
|---|---|---|
| $C_3S$ | 517 | Ref. 16* |
| $C_2S$ | 262 | Ref. 16 |
| $C_3A$ | 1144 | Ref. 16‡ |
| $C_4AF$ | 725 | Ref. 22§ |

*$w/c$ = 0.4 and $T$ = 21°C. ‡Assuming production of monosulfoaluminate phase. §$w/c$ = 0.5 and $T$ = 20°C.

To calibrate the model to the experimental results, both are fitted to the same functional form. In the literature, a variety of models have been used to fit either degree of hydration or strength development versus time,[51] mainly in connection with the application of the maturity method to concrete strength development. Two commonly used models are the linear- and parabolic-dispersion models originally developed by Knudsen.[52] The parabolic form of the model, which generally has been found to provide the better fit to the experimental data,[14] takes the form

$$A = A_u \frac{k(t - t_0)^{1/2}}{1 + k(t - t_0)^{1/2}} \tag{6}$$

where $A_u$ is the ultimate achievable value of the property, $t_0$ an induction time, and $k$ a rate constant. Equation (6) does not attempt to model degree of hydration, $\alpha$, during the early accelerator period of the cement hydration ($0 < \alpha < 0.15$), but generally provides an excellent fit to experimental data for $\alpha > 0.15$.[52]

Equation (6) has been fitted to the experimental nonevaporable water content data using nonlinear regression analysis available in DATAPLOT,[53] a graphical analysis software package developed at NIST. Although the 8 h data point for nonevaporable water content, generally corresponding to an $\alpha$ in the range 0.10–0.15, is slightly outside the range of application of the dispersion model recommended by Knudsen,[52] the fitted lines deviate little from these data values, suggesting that $\alpha > 0.10$ may be a more practical application range for Eq. (6). Figure 8 provides a representative example of the fit of Eq. (6) to the experimental data; for both cements, the fits in general are excellent. Table VII summarizes the results of the regression analysis, including the results generated at all three temperatures investigated in this study. For the 25°C results, the value of $t_0$ is relatively constant for a given cement at the three different *w/c* ratios.

### (2) Model Results

Some general results of the microstructure model are presented before proceeding to the comparison of model hydration rate, heat release, and chemical shrinkage to the experimental data. Results can be summarized conveniently by plotting the phase volume fraction versus the number of elapsed dissolution cycles for each phase present in the model. Typical results are illustrated in Figs. 9 through 11, which provide a series of graphs for Cement 116 at *w/c* = 0.40. For the anhydrous phases ($C_3S$, etc.), the phase fractions decrease monotonically with cycles, but at rates proportional to the assigned dissolution probabilities of the phase (i.e., $C_3S$ and $C_3A$ react at higher rates than $C_2S$ and $C_4AF$). Similarly, as shown in Fig. 10, porosity decreases monotonically with cycles. C-S-H, CH, and $FH_3$ increase monotonically with cycles.

The behavior of the aluminate hydration products is more complex, as shown in Fig. 11, for the first 800 cycles of hydration. Here, while gypsum remains in the system at a significant level (>10% of its initial volume), mostly ettringite (and a little $C_3AH_6$) is formed from the reaction of the aluminate phases with gypsum. When the gypsum is nearly consumed, the formation of the monosulfoaluminate phase (Afm) begins, and the supply of ettringite is gradually depleted, while more

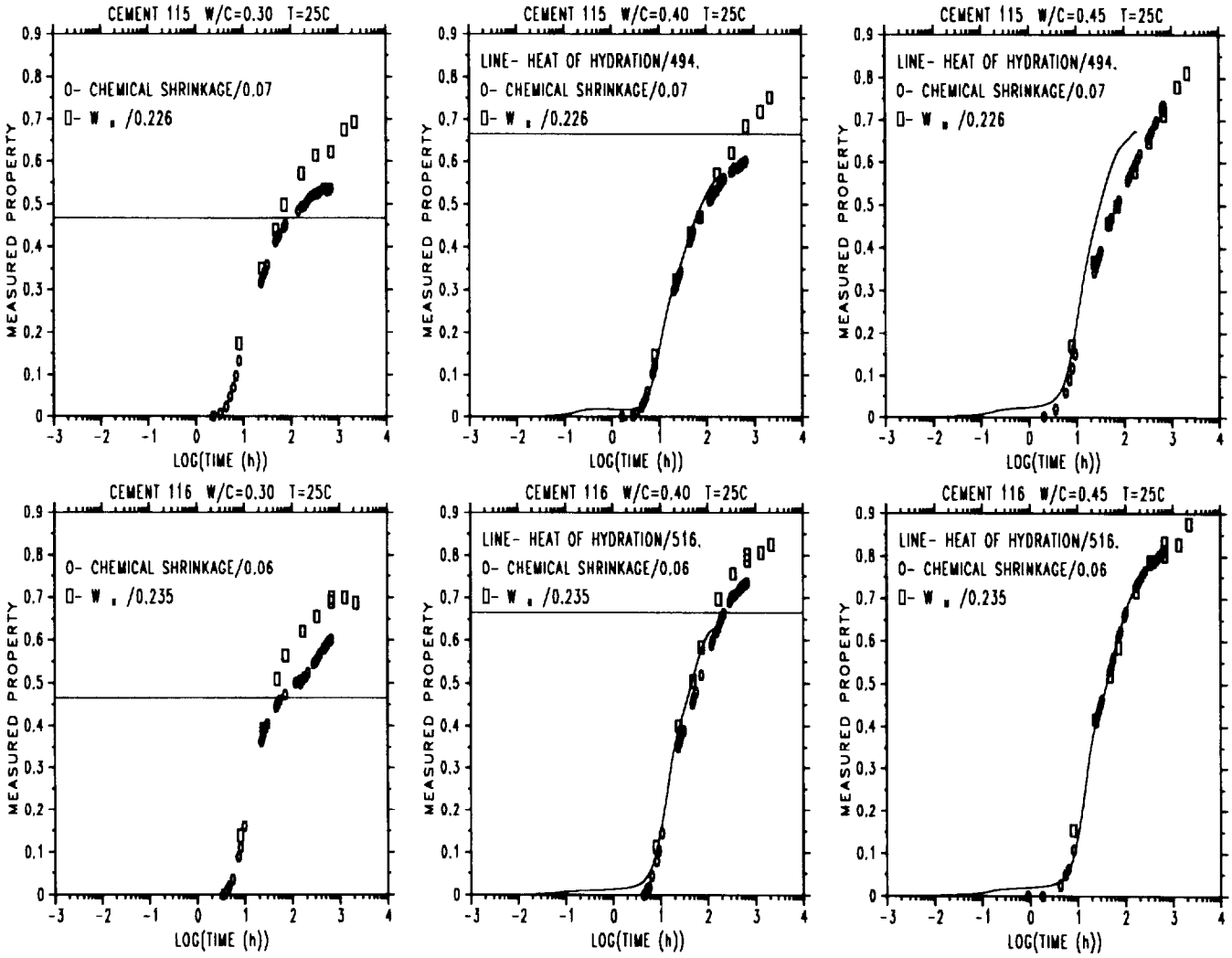


**Fig. 7.** Experimental results for CCRL Cements 115 and 116 versus time.

$C_3AH_6$ continues to form. The initiation of monosulfoaluminate formation prior to the complete depletion of gypsum is consistent with recent experimental results on the pure aluminate phases.[54] The shapes of the curves for the ettringite buildup and decay and the monosulfoaluminate buildup are quite similar to those found in the literature,[46] as measured using XRD on pastes in which the dissolution of the ferrite phase has been specially activated. The persistence of ettringite at long times also is consistent with the recent synchrotron radiation–energy-dispersive diffraction measurements of Henderson *et al.*,[55] who measured ettringite contents on the order of 7% after 326 d of hydration for a $w/c = 0.5$. This value is larger than those predicted by the model in the present study, which could be due in part to the lower sulfate content of the cements (~1.6% $SO_3$ versus the 2.7%–2.9% in Table I) used in the experimental study.[55]

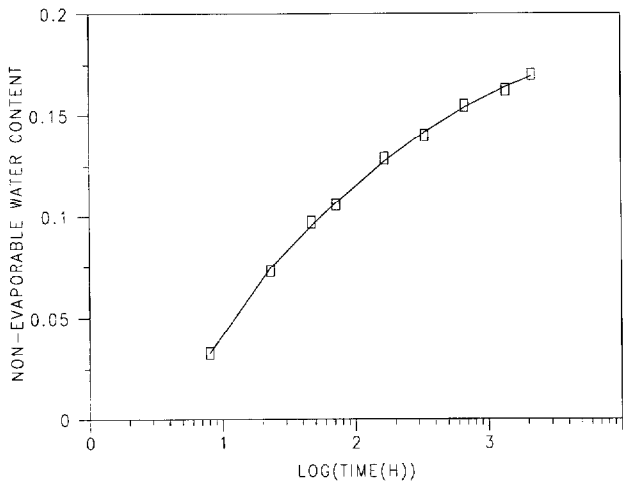


**Fig. 8.** Fit of Knudsen's parabolic dispersion model to experimental nonevaporable water content (g $H_2O$/(g cement)) versus time for Cement 115 with $w/c = 0.40$ and $T = 25°C$.

In Fig. 11, the ettringite peaks to a maximum volume fraction at ~60–70 cycles. Later results present the calibration of model cycles against experimental time; such results indicate that 60–70 cycles corresponds to ~12–15 h of real time for these cements. This is a reasonable time for the conversion of ettringite to monosulfoaluminate to begin, as indicated by a secondary peak in calorimetry measurements.[26] Such a shoulder (peak) on the heat release curve can be clearly observed for the heat release signal curve for Cement 116 in Fig. 3 (occurring at ~750 min). However, some researchers[56] have suggested that this secondary heat peak is associated with the renewed formation of ettringite and not the conversion of ettringite to monosulfoaluminate. It should be recognized that model parameters (gypsum and aluminate dissolution rates) can be adjusted to obtain this depletion of gypsum at any specific time. Here, the relative agreement with conventional experimental observations is rather fortuitous, because no specific attempt has been made to achieve this gypsum depletion at a specific time. Rather, the relative dissolution probabilities of the phases have

**Table VII. Parameters for Knudsen's Parabolic Dispersion Model for Cements 115 and 116**

| w/c | Temperature (°C) | $A_u$ (g $H_2O$/(g cement))† | $k$ ($h^{-1/2}$)† | $t_0$ (h)† |
|---|---|---|---|---|
| | | Cement 115 | | |
| 0.30 | 15 | 0.180 (0.007) | 0.124 (0.014) | 7.3 (0.5) |
| 0.30 | 25 | 0.171 (0.003) | 0.218 (0.017) | 6.2 (0.5) |
| 0.30 | 35 | 0.159 (0.002) | 0.359 (0.025) | 5.4 (0.5) |
| 0.40 | 15 | 0.215 (0.003) | 0.089 (0.004) | 6.9 (0.3) |
| 0.40 | 25 | 0.193 (0.002) | 0.154 (0.005) | 6.2 (0.2) |
| 0.40 | 35 | 0.180 (0.002) | 0.272 (0.014) | 4.8 (0.5) |
| 0.45 | 15 | 0.218 (0.008) | 0.099 (0.012) | 7.0 (0.6) |
| 0.45 | 25 | 0.207 (0.003) | 0.145 (0.008) | 5.4 (0.5) |
| 0.45 | 35 | 0.185 (0.002) | 0.271 (0.013) | 5.0 (0.4) |
| | | Cement 116 | | |
| 0.30 | 15 | 0.196 (0.005) | 0.139 (0.011) | 7.6 (0.2) |
| 0.30 | 25 | 0.181 (0.004) | 0.299 (0.031) | 7.5 (0.2) |
| 0.30 | 35 | 0.183 (0.001) | 0.372 (0.013) | 5.2 (0.2) |
| 0.40 | 15 | 0.232 (0.009) | 0.103 (0.012) | 7.5 (0.4) |
| 0.40 | 25 | 0.221 (0.004) | 0.197 (0.016) | 7.5 (0.2) |
| 0.40 | 35 | 0.211 (0.004) | 0.304 (0.032) | 5.4 (0.7) |
| 0.45 | 15 | 0.247 (0.007) | 0.106 (0.009) | 7.5 (0.3) |
| 0.45 | 25 | 0.231 (0.005) | 0.187 (0.016) | 7.0 (0.4) |
| 0.45 | 35 | 0.226 (0.006) | 0.275 (0.035) | 5.3 (0.9) |

†Numbers in parentheses indicate approximate standard deviation provided by DATAPLOT.[53]

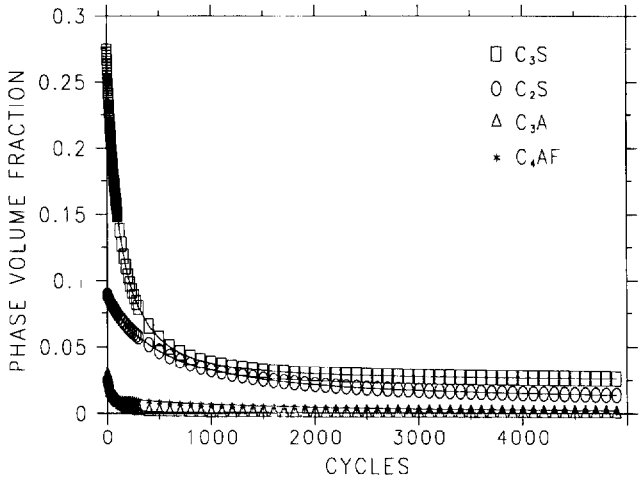


**Fig. 9.** Model anhydrous cement volume fractions versus elapsed cycles for Cement 116 with $w/c = 0.40$.

been set a priori at reasonable values based on data in the literature.[26]

### *(3) Calibration of Experimental to Model Predictions*

To fit the model results to those measured experimentally, a conversion between cycles and time is necessary. The simplest conversion would be to use a linear proportionality (time = $B \times$ cycles). However, it has been pointed out previously to the author that, if one assigns unit real time to each iteration of the NIST cement hydration model, linear kinetics are generated that closely follow Knudsen's linear dispersion model.[57] But, because experimental observations largely indicate parabolic hydration kinetics, a better match between model kinetics and experiment has been sought by investigating an alternative iteration–time mapping, namely

$$\text{time(h)} = t_0 + B \times (\text{cycles})^2 \tag{7}$$

with the $t_0$ term (from Table VII) included because the current version of the cement hydration model covers only the post-induction period. In this way, the linear kinetics obeyed by the model can be adapted to the parabolic kinetics exhibited by the real cements.

To calibrate the model to the experimental results based on the nonevaporable water content data, the model results for

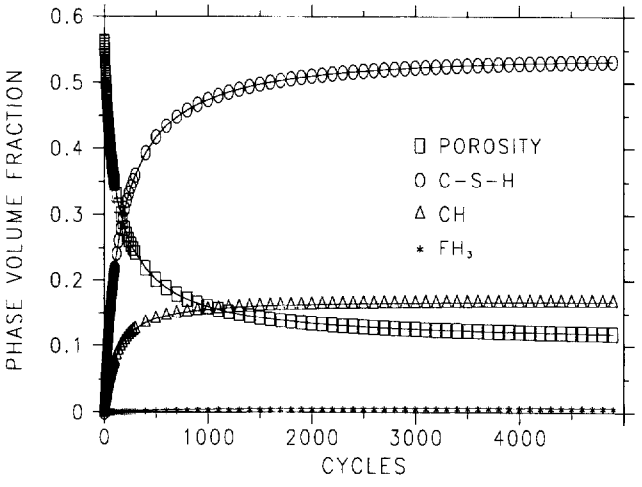


**Fig. 10.** Model porosity and reaction product volume fractions versus elapsed cycles for Cement 116 with $w/c = 0.40$.

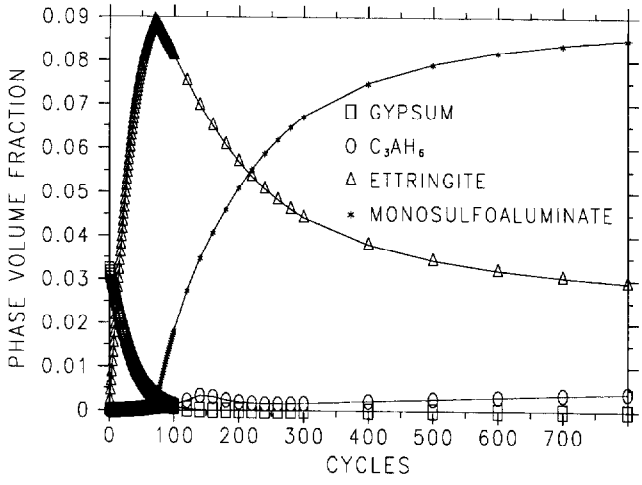


**Fig. 11.** Model aluminate reaction product volume fractions versus elapsed cycles for Cement 116 with $w/c = 0.40$.

**Table VIII. Parameter for Converting Cycles to Time for Cements 115 and 116**

| Cement | *w/c* | *B* |
|---|---|---|
| 115 | 0.30 | 0.0014 |
| 115 | 0.40 | 0.0023 |
| 115 | 0.45 | 0.0020 |
| 116 | 0.30 | 0.0013 |
| 116 | 0.40 | 0.0016 |
| 116 | 0.45 | 0.0016 |

degree of hydration have been regressed in Eq. (6) using the earlier deduced parameters for $A_u$ and $k$, and a subset of the model degree-of-hydration data. This subset has been generated by selecting single data points at ~0.05 degree-of-hydration intervals for values of degree of hydration between 0.10 and the amount of hydration achieved experimentally at 90 d. In this way, the regression being applied to the model is being weighted in approximately the same manner as that which has been applied to the experimental results. This step is deemed necessary because the model degree of hydration values are not evenly distributed with number of cycles (i.e., more hydration occurs during the early cycles than during the later ones). The previously determined value of $A_u$ has been converted to a degree of hydration, via normalization by the value for the nonevaporable water content at complete hydration (0.226 or 0.235). The coefficients determined for $B$ as a function of cement and *w/c* ratio are summarized in Table VIII. Interestingly, the values for $B$ are relatively constant, suggesting that a constant value of $B$ (such as the average $B$ value of 0.0017) can serve to model all of the results for the two cements and three *w/c* ratios. From the variability in the results in Table VII, an average value of $t_0$ (namely 6.7 h) also may suffice for these two particular cements at 25°C. This value is slightly larger than the final times of set measured for the two cements using the Vicat and Gillmore needle techniques, which are both on the order of 5 h.[20]

Once a value(s) of $B$ has been determined, plots comparing model and experimental results can be generated. Figures 12 through 14 provide example fits of the model to the experimental data for Cement 115 with *w/c* = 0.40. In these figures, the solid lines indicate the model data obtained using the specific

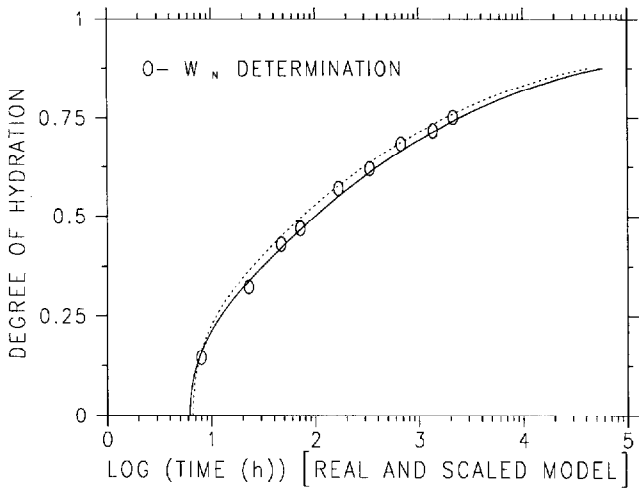


**Fig. 12.** Measured and model degree of hydration versus time for Cement 115 with *w/c* = 0.40.

values of $t_0$ and $B$ for *w/c* = 0.40 for Cement 115, as given in Tables VII and VIII, and the dotted lines indicate the results that would be obtained using single average values for these parameters regardless of *w/c* ratio and cement identification. Figures 12 through 14 show that the agreement between the solid lines and the experimental data is, in general, excellent. For the other *w/c* ratios and for Cement 116, the quality of the fits is similar to that exhibited in Figs. 12 through 14. For the dotted lines, the agreement is similar, suggesting that, for these two cements, a single relationship can be used to convert model cycles into real time. This suggests that, by capturing the particle-size distribution and phase distributions of the cements, much of the hydration kinetics behavior is implicitly included in the hydration model; i.e., the initial cement particle microstructure has a large influence on the postinduction period kinetics of cement hydration. Thus, a calibration performed for one cement at one *w/c* ratio can be used to predict the hydration behavior of other cements, of reasonably similar phase composition, at a variety of *w/c* ratios.

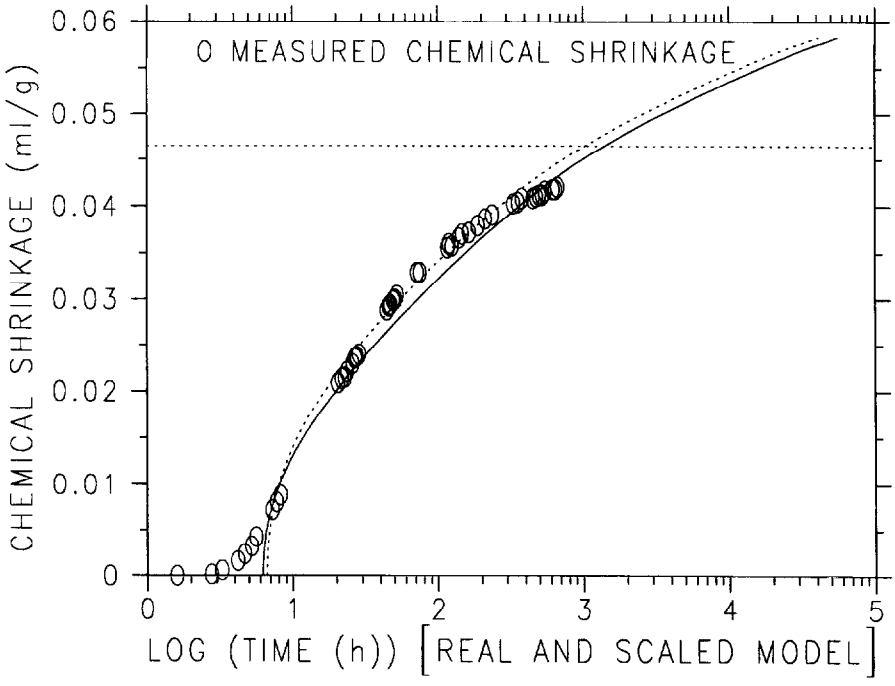


**Fig. 13.** Measured and model chemical shrinkage versus time for Cement 115 with *w/c* = 0.40.

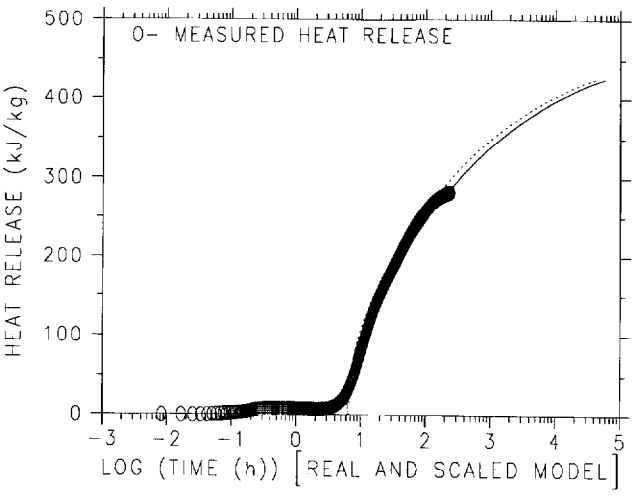


**Fig. 14.** Measured and model heat release versus time for Cement 115 with $w/c = 0.40$.

### *(4) Prediction of Compressive Strength*

In terms of performance variables, one important property is the compressive strength. Previously, Osbaeck and Johansen[58] developed a mathematical model relating cement particle-size distribution to strength development. Assuming that the depth of the hydrated layer is independent of particle diameter (which also is assumed tacitly in the NIST cement hydration model) and proportional to the square root of time, they were able to quantitatively predict the effects of particle-size distribution on strength evolution. More recently, Tsivilis and Parissakis[59] also showed that cement fineness is an important factor influencing compressive strength, with phase compositions becoming significant at later ages. In this study, we also have attempted to predict the compressive strength development of standard ASTM C 109[14] mortar cubes, making use of the gel-space ratio concept of Powers and Brownyard.[35] The gel-space ratio is defined by[35]

$$X = \frac{0.68\alpha}{0.32\alpha + \frac{w}{c}} \tag{8}$$

where $\alpha$ is the degree of hydration. It has been shown that the compressive strength of ASTM C 109 mortar cubes ($\sigma_c$) at any age ($t$) can be related to this gel-space ratio in the following manner:[35]

$$\sigma_c(t) = \sigma_A X(t)^n \tag{9}$$

where $\sigma_A$ represents the intrinsic strength of the cement and $n$ takes on values between 2.6 and 3.0, depending on the cement being investigated. Powers and Brownyard observed the value of $\sigma_A$ to be lower for cements with higher Bogue potential $C_3A$ contents (e.g., >7%).[35] Recently, Radjy and Vunic[60] showed that the gel-space ratio can be used to predict the compressive strength development of concrete based on measuring the adiabatic heat signature to estimate the degree of hydration.

Based on ASTM C 109,[21] test mortars were prepared with $w/c = 0.485$ for portland cement materials. Thus, model cements with $w/c = 0.485$ were generated for Cements 115 and 116 using the previously described computational techniques. Because no experimental nonevaporable water content data were available, the values of $t_0$ and $B$ determined for each of the two cements at $w/c = 0.45$ were used to convert model cycles to time based on Eq. (7). From the CCRL test program, compressive strengths at 3, 7, and 28 d were available. The NIST cement hydration model was utilized to compute the expected degree of hydration for these cements at 3, 7, and 28 d, so that $X$ could be computed according to Eq. (8). The 3 d measured compressive strength then was used to determine the value of $\sigma_A$ in Eq. (9), assuming an exponent $n$ of 2.6. Values of

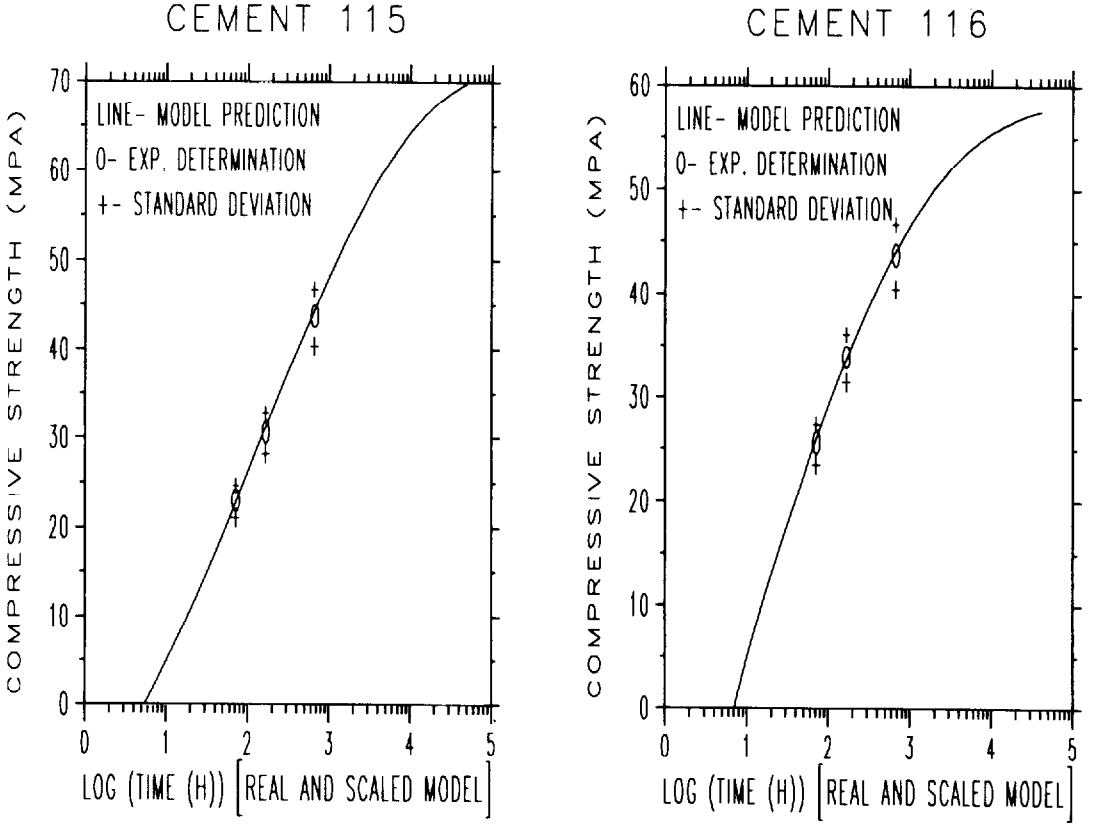


**Fig. 15.** Predicted and measured compressive strength development for Cements 115 and 116.

**Panel D: Maturity Method**

The maturity method has been developed to provide a quantitative technique for predicting the in-place compressive strength development of a concrete, based on its thermal history.[62] Because strength is strongly linked to the amount of cement that has reacted (degree of hydration), this approach should also be applicable to predicting the effects of temperature on hydration kinetics. In fact, the expressions commonly used in the maturity method to relate strength to time[51] are equivalent to the dispersion models of Knudsen,[52] which are being used in the present study to relate degree of hydration to time. Basically, the maturity method accounts for the time–temperature history of the curing of a concrete by determining a relationship between temperature and a rate constant, typically a rate constant for compressive strength development, but, in our case, one for degree of hydration development ($k$ in Table VII).

Typically, an Arrhenius function of the form

$$k = k_0 \exp(-E_a/RT) \tag{10}$$

is fitted to the values of the rate constant $k$ versus temperature, such as those provided in Table VII. In Eq. (10), $T$ is the absolute temperature (in kelvin), $R$ the universal gas constant (8.314 J/(mol·K)), and $E_a$ an *apparent* activation energy (typically in kJ/mol). Because the different mineral phases of a cement may react at different rates, implying a nonhomogeneous system, $E_a$ is not a true activation energy but, rather, provides an apparent value.[51] Based on Eq. (10) a plot of ln $k$ vs $1/T$ should give a straight line whose slope is proportional to $E_a$. Although alternatives to the Arrhenius equation, such as a simple exponential function (e.g., $k = A_0 \exp(BT)$, $T$ in °C), have been explored previously,[51] for this study, the Arrhenius equation generally was found to provide the better fit (smaller residual standard deviation) to the data. Once $k$ has been determined as a function of temperature, then, at any temperature of interest ($T_i$) an equivalent time ($t_e$) can be calculated relative to a reference temperature ($T_r$, 25°C in this study), as

$$t_e = \frac{k_T}{k_r} t = \exp\left[-\frac{E_a}{R}\left(\frac{1}{T_i} - \frac{1}{T_r}\right)\right] t \tag{11}$$

where $k_T$ is the rate constant at the experimental temperature of interest, $k_r$ the rate constant at the reference temperature, and $t$ the elapsed time at the experimental temperature. In this way, time values at which degree of hydration has been measured at any temperature can be converted to equivalent times at 25°C, so that data obtained at various temperatures can be plotted on a single equivalent time axis, in hopes of obtaining a single curve for degree of hydration versus equivalent time.

$\sigma_A$ of 129 and 99 MPa were thus determined for Cements 115 and 116, respectively. As noted above, Cement 116, with the higher $C_3A$ content, was observed to have the lower intrinsic strength.

Once $\sigma_A$ was determined, the model could be used to predict $\sigma_c$ at 7 and 28 d for comparison to the experimental data. Figure 15 presents the predicted strength developments in comparison to those measured in the CCRL proficiency sample program.[20] The standard deviation in the measured values also is included in the plots for reference purposes. The predictive ability of the model again is demonstrated, because it appears that compressive strength can be predicted well within the standard deviation of an interlaboratory test program. Because the model explicitly accounts for the particle-size distribution and phase composition of a cement, these results suggest that these parameters affect strength mainly through their influence on the hydration kinetics of the cement paste, because Eqs. (8) and (9) are based only on the degree of hydration and $w/c$ ratio of the system.

### *(5) Effects of Temperature*

Table VII also contains the values of $A_u$, $k$, and $t_0$ determined via the nonevaporable water content measurements at 15° and 35°C. As would be expected, the rate constant ($k$) is a strong function of temperature. In addition, the induction period ($t_0$) decreases slightly with increasing temperature, as does the value of the asymptotic nonevaporable water content ($A_u$). Geiker[29] has noted a similar trend for the values of $A_u$, quoting values of 0.206, 0.201, and 0.198 g of $H_2O$/(g of cement) for curing temperatures of 20°, 35°, and 50°C, respectively, for a rapid hardening portland cement with $w/c = 0.45$, based on the data of Munkholt.[61]

Perhaps the simplest method for relating model results calibrated at 25°C to other temperatures is through the use of a maturity-type approach[51,62] (see Panel D). Table IX summarizes the values determined, using this approach, for the apparent activation energies for the rate of hydration for Cements 115 and 116 for the three $w/c$ ratios investigated in this study. The values, all in the range of 35–42 kJ/mol, are in good agreement with those previously determined for cementitious systems, as summarized by Tank and Carino.[44]

Using the average value of the activation energies given in Table IX, 38.2 kJ/mol, multiplicative factors of 0.585 and 1.65 would be necessary to convert the curing times at 15° and 35°C to equivalent times at 25°C, respectively. Using these two values, Fig. 16 provides plots of the degree of hydration, estimated via the nonevaporable water content, versus time for the two cements and three $w/c$ ratios. In every case, using the equivalent time concept collapses the three data sets onto a single master curve. Although some dispersion is seen at longer times, in general, the three data sets asymptotically approach about the same value for degree of hydration, for a fixed cement and $w/c$ ratio.

Based on a simple application of the gel-space ratio concept described previously, one would expect that these systems might also have the same ultimate strength values. This, however, is in contrast to measured compressive strength values for concretes with $w/c \geq 0.45$,[62,63] where the ultimate strength is significantly higher the lower the curing temperature (e.g., the ultimate strength for a concrete cured at 10°C may be 180% of that for an equivalent concrete cured at 40°C). The most likely explanation for this discrepancy is that the intrinsic strength of the cement hydrates is a function of curing temperature. This would change the value of $\sigma_A$ in Eq. (9) and alter the values of the coefficients used in Eq. (8). Because Geiker[29] has noted that the measured chemical shrinkage is significantly less for

**Table IX. Apparent Activation Energies for Hydration of Cements 115 and 116 as Determined by the Maturity-type Approach**

| Cement | $w/c$ | Activation energy (kJ/mol)† |
|---|---|---|
| 115 | 0.30 | 39.3 (0.6) |
| 115 | 0.40 | 41.3 (1.2) |
| 115 | 0.45 | 36.9 (6.0) |
| 116 | 0.30 | 36.5 (11) |
| 116 | 0.40 | 40.0 (3.8) |
| 116 | 0.45 | 35.3 (3.2) |

†Numbers in parentheses indicate approximate standard deviation provided by DATAPLOT.[53]

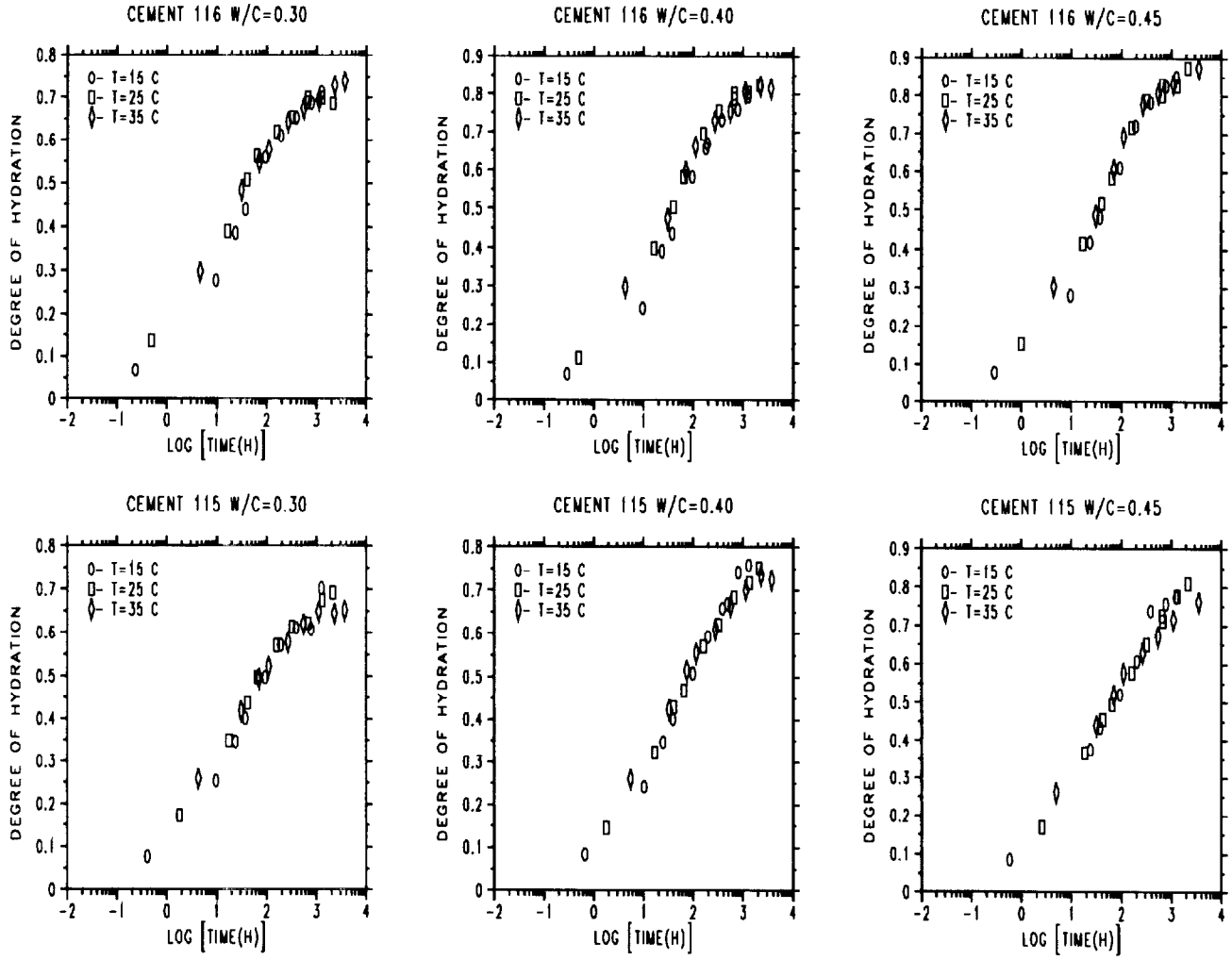


**Fig. 16.** Superposition of degree of hydration results at three temperatures for CCRL Cements 115 and 116.

samples cured at elevated temperatures, it would seem likely that the C-S-H gel formed at higher temperatures is incorporating less water into its gel structure, in turn implying a denser gel. This increased density of the C-S-H gel also would be consistent with the increased and coarser capillary porosity measured on samples cured at higher temperatures.[64,65] In this case, to truly model the effects of temperature on hydration and microstructure, the stoichiometry, molar volume, and density of the C-S-H phase should be a function of curing temperature. However, if one's main interest is in predicting degree of hydration, the maturity-type approach coupled with the current version of the NIST cement hydration model appears to be adequate, based on the results in Figs. 12 and 16.

### *(6) Effects of Sealed Hydration*

In addition to temperature, another material environmental condition variable of interest in hydration studies is the moisture content of the cement paste. Because cement hydration is generally viewed as a dissolution–precipitation process, the availability of water in the capillary pore space is paramount. As indicated by the chemical shrinkage measurements presented above, in a sealed system, empty pores are created as the hydration proceeds. This in turn would be expected to affect the kinetics of the hydration because of changes in solution concentrations and the reduction in available volume into which reaction products can precipitate. Modeling of this behavior is especially important for high-performance concretes, which often are based on mixture proportions with $w/c \leq 0.35$, because of the expected reduction in hydration (and strength) relative to saturated curing, and because the menisci created as the pores empty induce drying (self-desiccation) shrinkage stresses within the microstructure,[66,67] even before the material's strength is fully developed.

To preliminarily test the capability of the NIST cement hydration model to effectively reproduce the effects of self-desiccation on hydration kinetics, the model was executed for

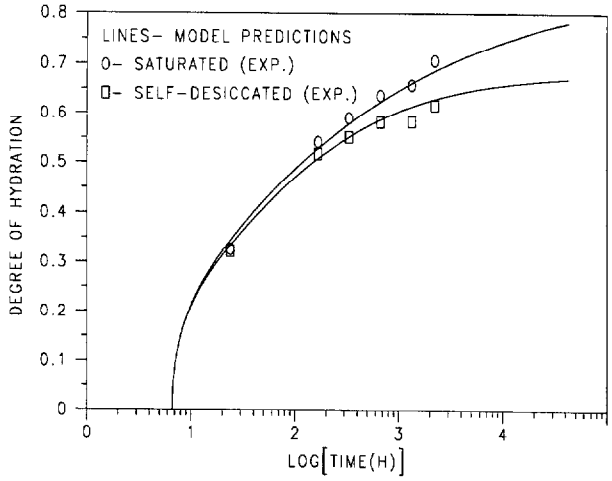


**Fig. 17.** Predicted and measured degrees of hydration for Cement 115 with $w/c = 0.30$ hydrated under sealed and saturated conditions at 25°C.

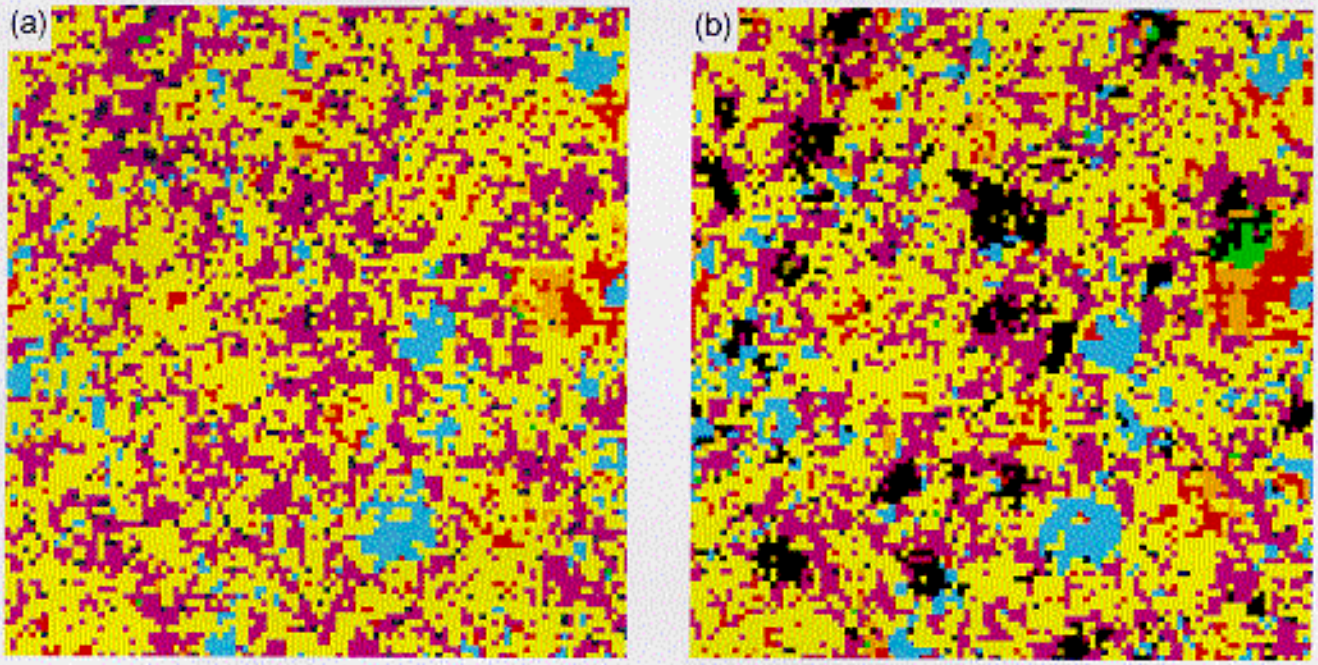


**Fig. 18.** Comparison of hydrated microstructures for hydration under (a) saturated and (b) sealed conditions ($C_3S$ is red, $C_2S$ is aqua, $C_3A$ is green, $C_4AF$ is orange, gypsum is pale green, C-S-H is yellow, other hydration products are magenta, water-filled porosity is blue, and empty porosity is black).

Cement 115 with $w/c = 0.30$ under conditions in which no external water was available, so that empty pores were created as the hydration proceeded as described in the Computational Techniques section. In addition, experimental measurements were made under both saturated and sealed conditions. Figure 17 provides a comparison of the experimental measurements and model predictions for degree of hydration versus time for these two systems. Model cycles were converted to time using values of $B = 0.0017$ and $t_0 = 6.7$. Once again, the model was found to reproduce the experimentally observed difference in hydration kinetics due to the self-desiccating conditions. Early in the hydration process, the kinetics were not influenced strongly because sufficient water was present and few empty pores existed. However, as hydration continued, the empty pores occupied an ever-increasing fraction of the remaining total porosity, resulting in a significant decrease in achieved degree of hydration. This is shown clearly in Fig. 18, which compares two-dimensional slices from the same $z$-plane after 5000 cycles of hydration under both saturated and sealed conditions. Substituting the 90 d value of $\alpha$ into Eqs. (8) and (9), one finds a reduction in predicted 90 d compressive strength from 102 to 83 MPa, a reduction of ~20%, emphasizing the importance of the proper curing of low $w/c$ ratio concretes. If an accurate model could be developed for the drying kinetics of a hydrating cement paste, it should be possible to extend the cement hydration model to consider hydration of cement paste exposed to different external relative humidities, in addition to the saturated and sealed conditions explored in this study.

## V. Conclusions

The results presented in this paper illustrate the importance of the physical microstructure (particle-size distributions and phase fractions and distributions) of the initial cement powder in influencing the hydration kinetics of cement paste. This emphasizes the necessity of an accurate and quantitative characterization of the starting materials to develop a realistic hydration model. The development of a three-dimensional computer model utilizing realistic starting microstructures has been shown to provide quantitative predictions of the effects of cement composition, water-to-cement ($w/c$) ratio, and curing environment on resultant hydration and physical properties, such as heat release and mortar cube compressive strength. In general, for the two cements examined in this study, once a calibration is performed for one cement and $w/c$ ratio, the predictive ability of the model for other systems is excellent, suggesting that the model may be applicable in designing new materials. Future efforts will concentrate on the incorporation of mineral admixtures, such as silica fume and fly ash, and the addition of one or more computer modules to model the early time (induction period) hydration behavior, so that the length of the induction period can be predicted as well.

**Acknowledgments:** The author would like to thank Paul Stutzman of BFRL (NIST) for acquiring the two-dimensional SEM images of the CCRL cements, Wei-Guo Lei of the University of Illinois for measuring their particle-size distributions, Robin Haupt of CCRL for supplying samples of the cements and results collected from their proficiency sample program, and Ken Snyder of BFRL for useful discussions and assistance with the nonevaporable water content measurements.

## References

[1]D. P. Bentz and E. J. Garboczi, "Modelling the Leaching of Calcium Hydroxide from Cement Paste: Effects on Pore Space Percolation and Diffusivity," *Mater. Struct.*, **25**, 523–33 (1992).

[2]D. P. Bentz, E. J. Garboczi, and N. S. Martys, "Application of Digital-Image-Based Models to Microstructure, Transport Properties, and Degradation of Cement-Based Materials"; pp. 167–85 in *The Modelling of Microstructure and Its Potential for Studying Transport Properties and Durability*. Edited by H. M. Jennings, J. Kropp, and K. L. Scrivener. Kluwer Academic Publishers, Dordrecht, The Netherlands, 1996.

[3]F. H. Wittmann, P. E. Roelfstra, and H. Sadouki, "Simulation and Analysis of Composite Structures," *Mater. Sci. Eng.*, **68**, 239–48 (1984–1985).

[4]P. E. Roelfstra, H. Sadouki, and F. H. Wittmann, "Le Beton Numerique (Numerical Concrete)," *Mater. Struct.*, **18**, 327–35 (1985).

[5]H. M. Jennings and S. K. Johnson, "Simulation of Microstructure Development During the Hydration of a Cement Compound," *J. Am. Ceram. Soc.*, **69**, 790–95 (1986).

[6]D. Viehland, J. F. Li, L. J. Yuan, and Z. Xu, "Mesostructure of Calcium Silicate Hydrate (C-S-H) Gels in Portland Cement Paste: Short-Range Ordering, Nanocrystallinity, and Local Compositional Order," *J. Am. Ceram. Soc.*, **79** [7] 1731–44 (1996).

[7]K. Van Breugel, "Simulation of Hydration and Formation of Structure in Hardening Cement-Based Materials"; Ph.D. Thesis. Delft University of Technology, Delft, The Netherlands, 1991.

[8]K. Van Breugel, "Models for Prediction of Microstructural Development in Cement-Based Materials"; see Ref. 2, pp. 91–106.

[9]P. Navi and C. Pignat, "Simulation of Effects of Small Inert Grains on Cement Hydration and Its Contact Surfaces"; see Ref. 2, pp. 227–40.

[10]Y. Xi, P. D. Tennis, and H. M. Jennings, "Mathematical Modeling of Cement Paste Microstructure by Mosaic Pattern: Part I. Formulation," *J. Mater. Res.*, **11** [8] 1943–52 (1996).

[11]D. P. Bentz and E. J. Garboczi, "Percolation of Phases in a Three-Dimensional Cement Paste Microstructural Model," *Cem. Concr. Res.*, **21** [2] 325–44 (1991).

[12]D. P. Bentz, P. Coveney, E. J. Garboczi, M. Kleyn, and P. E. Stutzman, "Cellular Automaton Simulations of Cement Hydration and Microstructure Development," *Modell. Simul. Mater. Sci. Eng.*, **2** [4] 783–808 (1994).

[13]D. P. Bentz and E. J. Garboczi, "Guide to Using HYDRA3D: A Three-Dimensional Digital-Image-Based Cement Microstructural Model," NISTIR No. 4746, U.S. Department of Commerce, Washington, DC, 1992.

[14]D. P. Bentz, "A Three-Dimensional Cement Hydration and Microstructure Program. I. Hydration Rate, Heat of Hydration, and Chemical Shrinkage," NISTIR No. 5756, U.S. Department of Commerce, Washington, DC, Nov. 1995.

[15]F. Tzschichholz, H. J. Herrmann, and H. Zanni, "Reaction–Diffusion Model for the Hydration and Setting of Cement," *Phys. Rev. E: Stat. Phys., Plasmas, Fluids, Relat. Interdiscip. Top.*, **53** [3] 2629–37 (1996).

[16]E. J. Garboczi and D. P. Bentz, "Computer Simulation of the Diffusivity of Cement-Based Materials," *J. Mater. Sci.*, **27**, 2083–92 (1992).

[17]R. T. Coverdale, B. J. Christensen, J. M. Jennings, T. O. Mason, D. P. Bentz, and E. J. Garboczi, "Interpretation of Impedance Spectroscopy of Cement Paste via Computer Modeling Part I: Bulk Conductivity and Offset Resistance," *J. Mater. Sci.*, **30** [3] 712–19 (1995).

[18]D. P. Bentz, D. A. Quenard, V. Baroghel-Bouny, E. J. Garboczi, and H. M. Jennings, "Modelling Drying Shrinkage of Cement Paste and Mortar: Part I. Structural Models from Nanometres to Millimetres," *Mater. Struct.*, **28**, 450–58 (1995).

[19]E. J. Garboczi and D. P. Bentz, "Modelling of the Microstructure and Transport Properties of Concrete," *Constr. Bldg. Mater.*, **10** [5] 293–300 (1996).

[20]Cement and Concrete Reference Laboratory Proficiency Sample Program: Final Report on Portland Cement Proficiency Samples Number 115 and Number 116, Cement and Concrete Reference Laboratory, National Institute of Science and Technology, Gaithersburg, MD, March, 1995.

[21]"Compressive Strength of Hydraulic Cement Mortars," ASTM Designation C 109. *1992 Book of ASTM Standards*, Vol. 04.01. American Society for Testing and Materials, Philadelphia, PA.

[22]K. L. Scrivener, "The Microstructure of Anhydrous Cement and Its Effect on Hydration"; pp. 39–46 in *Proceedings, Materials Research Society Symposia*, Vol. 85. Edited by L. J. Struble and P. W. Brown. Materials Research Society, Pittsburgh, PA, 1987.

[23]P. E. Stutzman, "Cement Clinker Characterization by Scanning Electron Microscopy," *Cem. Concr. Aggregates*, **13** [2] 109–14 (1991).

[24]D. Bonen and S. Diamond, "Application of Image Analysis to a Comparison of Ball Mill and High-Pressure Roller Mill Ground Cement"; pp. 101–19 in *Proceedings of the 13th International Conference on Cement Microscopy*. International Cement Microscopy Association, 1991.

[25]D. P. Bentz and P. E. Stutzman, "SEM Analysis and Computer Modelling of Hydration of Portland Cement Particles"; pp. 60–73 in *Petrography of Cementitious Materials*. Edited by S. M. DeHayes and D. Stark. American Society for Testing and Materials, Philadelphia, PA, 1994.

[26]H. F. W. Taylor, *Cement Chemistry*; pp. 62–63. Academic Press, London, U.K., 1990.

[27]B. N. Taylor and C. E. Kuyatt, "Guidelines for Evaluating and Expressing the Uncertainty of NIST Measurement Results," NIST Technical Note No. 1297, U.S. Department of Commerce, Washington, DC, Sept. 1994.

[28]E. J. Prosen, P. W. Brown, G. J. Frohnsdorff, and F. L. Davis, "A Multichambered Microcalorimeter for the Investigation of Cement Hydration," *Cem. Concr. Res.*, **15**, 703–10 (1985).

[29]M. Geiker, "Studies of Portland Cement Hydration: Measurements of Chemical Shrinkage and a Systematic Evaluation of Hydration Curves by Means of the Dispersion Model"; Ph.D. Thesis. Technical University of Denmark, Copenhagen, Denmark, 1983.

[30]E. Tazawa, S. Miyazawa, and T. Kasai, "Experimental Study on Mechanism of Autogeneous Shrinkage of Concrete," *Cem. Concr. Res.*, **25**, 288–92 (1995).

[31]J. G. Berryman, "Measurement of Special Correlation Functions Using Image Processing Techniques," *J. Appl. Phys.*, **57** [7] 2374–84 (1985).

[32]A. M. Law and W. D. Kelton, *Simulation Modeling and Analysis*; pp. 258–59. McGraw-Hill, New York, 1982.

[33]D. P. Bentz, E. J. Garboczi, P. J. P. Pimentia, and W. C. Carter, "Cellular Automaton Simulations of Surface Mass Transport Due to Curvature Gradients: Simulation of Sintering"; pp. 413–18 in *Synthesis and Processing of Ceramics: Scientific Issues*, Vol. 249. Materials Research Society, Pittsburgh, PA, 1992.

[34]J. W. Bullard, E. J. Garboczi, W. C. Carter, and E. R. Fuller, "Numerical Methods for Computing Interfacial Mean Curvature," *Comput. Mater. Sci.*, **4**, 1–14 (1995).

[35]S. Mindess and J. F. Young, *Concrete*. Prentice-Hall, Englewood Cliffs, NJ, 1981.

[36]J. F. Young and W. Hansen, "Volume Relationship for C-S-H Formation Based on Hydration Stoichiometry"; pp. 313–22 in *Microstructural Development During Hydration of Cement*, Vol. 235. Materials Research Society, Pittsburgh, PA, 1986.

[37]M. Fukuhara, S. Goto, K. Asaga, M. Daimon, and R. Kondo, "Mechanisms and Kinetics of $C_4AF$ Hydration with Gypsum," *Cem. Concr. Res.*, **11**, 407–14 (1981).

[38]*Handbook of Chemistry and Physics*, 63rd ed; pp. D52–D95. CRC Press, Boca Raton, FL, 1982.

[39]T. C. Powers, "Adsorption of Water by Portland Cement Paste during the Hardening Process," *Ind. Eng. Chem.*, **27**, 790–94 (1935).

[40]J. Gutowitz (Ed.), *Cellular Automata: Theory and Experiment*. MIT Press, Cambridge, MA, 1991.

[41]S. Wolfram, *Theory and Applications of Cellular Automata*. World Scientific, Singapore, 1986.

[42]P. J. P. Pimentia, E. J. Garboczi, and W. C. Carter, "Cellular Automaton Algorithm for Surface Mass Transport due to Curvature Gradients: Simulations of Sintering," *Comput. Mater. Sci.*, **1**, 63–77 (1992).

[43]J. A. Spittle and S. G. R. Brown, "A Cellular Automaton Model of Steady-State Columnar-Dendritic Growth in Binary Alloys," *J. Mater. Sci.*, **30**, 3989–94 (1995).

[44]S. G. R. Brown and N. B. Bruce, "Three-Dimensional Cellular Automaton Models of Microstructural Evolution During Solidification," *J. Mater. Sci.*, **30**, 1144–50 (1995).

[45]D. A. Young and E. M. Corey, "Lattice Models of Biological Growth," *Phys. Rev. A: Gen. Phys.*, **41** [12] 7024–32 (1990).

[46]W. Schwarz, "Novel Cement Matrices by Accelerated Hydration of the Ferrite Phase in Portland Cement via Chemical Activation: Kinetics and Cementitious Properties," *Adv. Cement-Based Mater.*, **2**, 189–200 (1995).

[47]A. M. Tenenbaum and M. J. Augenstein, *Data Structures Using Pascal*; pp. 230–38. Prentice-Hall, Englewood Cliffs, NJ, 1986.

[48]H. M. Jennings and L. J. Parrott, "Microstructural Analysis of Hardened Alite Paste, Part 2: Microscopy and Reaction Products," *J. Mater. Sci.*, **21**, 4053 (1986).

[49]L. J. Parrott, M. Geiker, W. A. Gutteridge, and D. Killoh, "Monitoring Portland Cement Hydration: Comparison of Methods," *Cem. Concr. Res.*, **20**, 919–26 (1990).

[50]R. A. Olson, B. J. Christensen, R. T. Coverdale, S. J. Ford, G. M. Moss, H. M. Jennings, T. O. Mason, and E. J. Garboczi, "Interpretation of the Impedance Spectroscopy of Cement Paste via Computer Modelling Part III: Microstructural Analysis of Frozen Cement Paste," *J. Mater. Sci.*, **30**, 5078–86 (1995).

[51]N. J. Carino, L. I. Knab, and J. R. Clifton, "Applicability of the Maturity Method to High-Performance Concrete," NISTIR No. 4819, U.S. Department of Commerce, Washington, DC, May 1992.

[52]T. Knudsen, "The Dispersion Model for Hydration of Portland Cement I. General Concepts," *Cem. Concr. Res.*, **14**, 622–30 (1984).

[53]J. J. Filliben, "DATAPLOT: Introduction and Overview," NBS Special Publication No. 667, U.S. Department of Commerce, Washington, DC, 1984.

[54]P. W. Brown, "Kinetics of Tricalcium Aluminate and Tetracalcium Aluminoferrite Hydration in the Presence of Calcium Sulfate," *J. Am. Ceram. Soc.*, **76** [12] 2971–76 (1993).

[55]E. Henderson, X. Turrillas, and P. Barnes, "The Formation, Stability, and Microstructure of Calcium Sulphoaluminate Hydrates Present in Hydrated Cement Paste, Using *in situ* Synchrotron Energy-dispersive Diffraction," *J. Mater. Sci.*, **30**, 3856–62 (1995).

[56]P. L. Pratt and A. Ghose, "Electron Microscope Studies of Portland Cement Microstructures during Setting and Hardening," *Philos. Trans. R. Soc. London*, **A310**, 93–103 (1983).

[57]T. Knudsen; personal communication, 1991.

[58]B. Osbaeck and V. Johansen, "Particle Size Distribution and Rate of Strength Development of Portland Cement," *J. Am. Ceram. Soc.*, **72** [2] 197–201 (1989).

[59]S. Tsivilis and G. Parissakis, "A Mathematical Model for the Prediction of Cement Strength," *Cem. Concr. Res.*, **25** [1] 9–14 (1995).

[60]F. F. Radjy and D. W. Vunic, "Heat Signature Testing of Concrete"; pp. 8–15 in *Proceedings of Structural Materials Technology—An NDT Conference* (Atlantic City, NJ, 1994). Techomic Publishing, Lancaster, PA, 1994.

[61]H. Munkholt, "Temperaturens Indflydelse paa Vands Fysiske Binding i Cement Pasta," 18-Points Report, The Institute of the Mineral Industry, Technical University of Denmark, Copenhagen, Denmark, 1983.

[62]R. C. Tank and N. J. Carino, "Rate Constant Functions for Strength Development of Concrete," *ACI Mater. J.*, **88** [1] 74–83 (1991).

[63]N. J. Carino, "The Maturity Method: Theory and Application," *Cem. Concr. Aggregates*, **6** [2] 61–73 (1984).

[64]A. Bentur, R. L. Berger, J. H. Kung, N. B. Milestone, and J. F. Young, "Structural Properties of Calcium Silicate Pastes: II, Effect of Curing Temperature," *J. Am. Ceram. Soc.*, **62** [7–8] 362–66 (1979).

[65]Y. Cao and R. J. Detwiler, "Backscattered Electron Imaging of Cement Pastes Cured at Elevated Temperatures," *Cem. Concr. Res.*, **25** [3] 627–38 (1995).

[66]C. Hua, P. Acker, and A. Erlacher, "Analyses and Models of the Autogeneous Shrinkage of Hardening Cement Paste," *Cem. Concr. Res.*, **25** [7] 1457–68 (1995).

[67]H. Justnes, A. Van Gemert, F. Verboven, and E. J. Sellevold, "Total and External Chemical Shrinkage of Low *w/c* Ratio Cement Pastes," *Adv. Cem. Res.*, **8** [31] 121–26 (1996). □

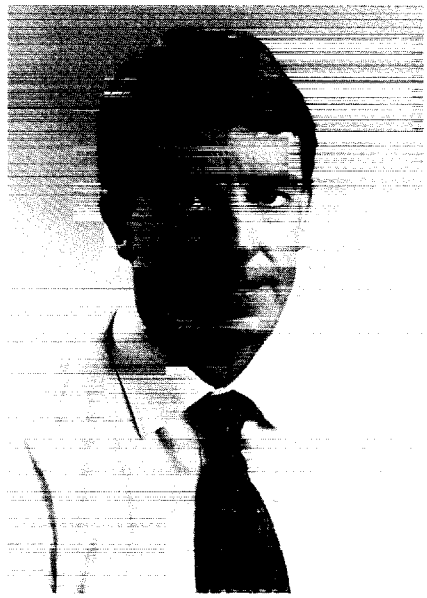

Dale P. Bentz is a chemical engineer in the Building Materials Division of the Building and Fire Research Laboratory at the National Institute of Standards and Technology, Gaithersburg, MD. His current research interests include fundamental experimental and computer modeling investigations of the hydration and microstructure of cement-based materials and the application of computer technology to building materials research. Mr. Bentz is the author or coauthor of more than 100 research papers. He is a member of the American Society for Testing and Materials (ASTM), the International Union of Testing and Research Laboratories for Materials and Structures (RILEM), and is currently chairperson of the Cements Division of the American Ceramic Society. He received a B.S. degree in chemical engineering from the University of Maryland (1984) and a M.S. degree in computer and information science from Hood College (1991).